



Cosmo-tomography toward PKS 1830-211: Variability of the quasar and of its foreground molecular absorption monitored with ALMA









Downloaded from: <https://research.chalmers.se>, 2025-12-04 14:33 UTC

Citation for the original published paper (version of record):

Muller, S., Marti-Vidal, I., Combes, F. et al (2023). Cosmo-tomography toward PKS 1830-211: Variability of the quasar and of its foreground molecular absorption monitored with ALMA. *Astronomy and Astrophysics*, 674.
<http://dx.doi.org/10.1051/0004-6361/202245768>

N.B. When citing this work, cite the original published paper.

Cosmo-tomography toward PKS 1830–211: Variability of the quasar and of its foreground molecular absorption monitored with ALMA

S. Muller¹, I. Martí-Vidal^{2,3}, F. Combes⁴, M. Gérin⁵, A. Beelen⁶, C. Horellou¹, M. Guélin⁷, S. Aalto¹,
J. H. Black¹, and E. van Kampen⁸

¹ Department of Space, Earth and Environment, Chalmers University of Technology, Onsala Space Observatory,
43992 Onsala, Sweden
e-mail: mullers@chalmers.se

² Departament d'Astronomia i Astrofísica, Universitat de València, C. Dr. Moliner 50, 46100 Burjassot, València, Spain

³ Observatori Astronòmic, Universitat de València, C. Catedrático José Beltrán 2, 46980 Paterna, València, Spain

⁴ Observatoire de Paris, LERMA, Collège de France, CNRS, PSL University, Sorbonne Université, Paris, France

⁵ LERMA, Observatoire de Paris, PSL University, CNRS, Sorbonne Université, 75014 Paris, France

⁶ Aix-Marseille Université, CNRS & CNES, Laboratoire d'Astrophysique de Marseille, 38, Rue Frédéric Joliot-Curie,
13388 Marseille, France

⁷ Institut de Radioastronomie Millimétrique, 300 Rue de la Piscine, 38406 Saint-Martin-d'Hères, France

⁸ European Southern Observatory, Karl-Schwarzschild-Str. 2, 85748 Garching b. München, Germany

Received 22 December 2022 / Accepted 10 April 2023

ABSTRACT

Context. Time variability of astronomical sources provides crude information on their typical size and on the implied physical mechanisms. PKS 1830–211 is a remarkable radio-bright lensed quasar with a foreground molecular absorber in the lens galaxy at $z = 0.89$. Small-scale morphological changes in the core–jet structure of the quasar – which is magnified by the lensing – result in a varying illumination of the absorber screen, which in turn causes variations in the absorption profile.

Aims. We aim to study the time variations of the system (the two main lensed images of the quasar and the two corresponding sight-lines in the absorber) in order to obtain constraints on both the quasar activity and small-scale structures in the interstellar medium of the absorber.

Methods. We used ALMA to monitor the submillimeter continuum emission of PKS 1830–211, together with the absorption spectra of the H_2O and CH molecules, with 17 visits spread over six months in 2016. Complementing this, we used available ALMA data to investigate changes in the system in the period 2012–2022.

Results. From the continuum data, we followed the evolution of the flux density, flux-density ratio, spectral index, and differential polarization between the two lensed images of the quasar; all quantities show significant variations related to the intrinsic activity of the quasar. We propose a simple parametric model of a core plus a ballistic plasmon to account for the continuum evolution, from which we constrain a time delay of 25 ± 3 days between main lensed images. The spectral lines reveal significant variations in the foreground absorption profile. A principal component analysis highlights apparent wavy time variations, possibly linked to the helical jet precession period of the quasar. From the deep averaged spectra towards the southwest image, we detect the absorption of the rare isotopolog ^{13}CH and estimate an abundance ratio of $^{12}\text{CH}/^{13}\text{CH} \sim 150$. We also measure the oxygen isotopic ratios, $^{16}\text{O}/^{18}\text{O} = 65.3 \pm 0.7$ and $^{18}\text{O}/^{17}\text{O} = 11.5 \pm 0.5$ in the $z = 0.89$ absorber. Finally, we find a remarkable continuous shallow trough in the water absorption spanning a velocity interval of nearly 500 km s^{-1} . This broad absorption could be the signature of an extra-planar molecular component.

Conclusions. All together, the system formed by the quasar PKS 1830–211 and its foreground lens–absorber acts as a powerful gravitational microscope, providing us with the possibility to dissect small-scale structures in both the ISM of the foreground absorber and the jet of the background quasar.

Key words. quasars: absorption lines – quasars: individual: PKS 1830–211 – gravitational lensing: strong – galaxies: ISM – galaxies: abundances – ISM: molecules

1. Introduction

Astronomical objects often appear to be of small angular size. Therefore, the study and characterization of these objects and of the inherent physical mechanisms (i.e., the whole subject of astrophysics) rely on our ability to access information corresponding to these small scales. This can be done in two ways: either with direct high-angular-resolution observations, for example by means of very long-baseline interferometry (VLBI), or, for varying sources, by studying their time variations

and their timescales. Using the causality argument, the typical timescale of signal variations should indeed reflect the size of the corresponding regions.

The time variability technique has been applied to various sources and contexts, including compact transient sources like transiting exoplanets, supernovae, pulsars, and black holes, to name but a few. For example, the reverberation mapping technique within the broad-line region in active galactic nuclei (AGN) provides size estimates from the line variability, which, combined with spectroscopy measurements of the

kinematics, yields a mass estimate for the central black hole (e.g., Bahcall et al. 1972; Blandford & McKee 1982). Another example is provided by the remarkable periodicity in the optical light curve of the gravitationally lensed quasar QJ0158–4325, which with the help of microlensing led (Millon et al. 2022) to propose a model based on a pair of supermassive black holes in the coalescence stage. Yet another application is the use of temporal variability of HI, optical, or ultraviolet absorption lines to study the small-scale structures down to a few AU in the interstellar medium (ISM; see e.g., a review by Stanimirović & Zweibel 2018).

The direction toward the lensed quasar PKS 1830–211, the subject of this work, is particularly favorable for studying time variability. PKS 1830–211 is a blazar at $z = 2.5$ (Lidman et al. 1999) with strong gravitational lensing due to an intervening nearly face-on spiral galaxy at $z = 0.89$ (Wiklind & Combes 1996; Winn et al. 2002). The blazar shows significant activity on short timescales (down to hours and days) when observed from radio waves to X- and γ -rays (e.g., Abdo et al. 2015; Martí-Vidal & Muller 2019; Martí-Vidal et al. 2020). Two factors boost the apparent variability of PKS 1830–211 from our viewpoint on Earth: (i) the orientation of the blazar’s relativistic jet close to the line of sight, which makes it prone to apparent superluminal motions, and (ii) the lensing and its associated source magnification. As a result of the lensing geometry, the quasar appears as two main bright and compact images (to the northeast and the southwest, hereafter the NE and SW images), separated by $\sim 1''$ and embedded in an Einstein ring with a steep spectral index (mostly seen at centimetre (cm) wavelengths; e.g., Jauncey et al. 1991), and a weak third lensed image at approximately the position of the lens galaxy (Muller et al. 2020a). There is a geometrical time delay of ~ 27 days between the NE (leading) and SW images (see Sect. 3.3).

In addition to the peculiarities of PKS 1830–211 mentioned above, the sightlines to the two main images intercept a molecular component in the disk of the $z = 0.89$ lens galaxy, causing a remarkable molecular absorption-line system (Wiklind & Combes 1998; Muller et al. 2014). A large number (>60) of molecules have been detected along the SW line of sight (e.g., Muller et al. 2011, 2014; Tercero et al. 2020), which have been used not only to investigate the chemical and isotopic composition of the gas in the absorber but also as sensitive cosmological probes; for example, of the cosmic microwave background temperature (Muller et al. 2013) and invariance of fundamental constants (e.g., Bagdonaite et al. 2013; Kanekar et al. 2015; Muller et al. 2021). However, these studies can be affected by systematic uncertainties due to the peculiarity of PKS 1830–211, with time variations being one of the major effects (e.g., Muller et al. 2021).

VLBI observations have revealed micro-changes in the morphology of the quasar on the timescale of months (Garrett et al. 1997). Furthermore, the apparent separation between the two lensed images has been measured to vary by up to $200 \mu\text{as}$ within eight months (Jin et al. 2003), which was interpreted by Nair et al. (2005) as evidence for recurrent plasmon ejections along a helical jet, with a jet precession period of one year. In addition, there is evidence for micro-lensing events in the X-ray and γ -ray light curves (e.g., Oshima et al. 2001; Neronov et al. 2015), implying that the hard emission is produced in the vicinity of the supermassive black hole.

These changes in the morphology of the quasar lead to variation in the illumination of the foreground material in the lens-absorber, and significant variation in the absorption profiles of molecular lines has been reported between spectra taken months

to years apart at millimeter (mm) wavelengths (Muller & Guélin 2008; Muller et al. 2014, 2021; Schulz et al. 2015). In contrast, there seems to be no line variability at cm wavelengths: Allison et al. (2017) and Combes et al. (2021) reported no significant variation in the redshifted HI 21-cm and OH lines between observations made at up to 20 year time intervals. This could be explained if the HI gas is distributed on larger scales than that probed by the changes in the source structure at these wavelengths. Regarding variations of absorption lines, the situation is indeed more favorable for molecular lines at high frequencies (i.e., in the mm/submm part of the electromagnetic spectrum): the background continuum emission is smaller (e.g., Guirado et al. 1999) and originates closer to the base of the jet; in addition, the molecular screen is expected to be more clumpy and to have a smaller scale height than the atomic screen.

Overall, PKS 1830–211, with its sustained blazar activity, its low-inclination jet with superluminal motions, its lens magnification, potential micro-lensing events, and its intervening lens-absorber with absorption profile variability, is thus a particularly interesting source for time monitoring. In this work, we present the results of a monitoring of the continuum activity of PKS 1830–211 and of H_2O and CH submm absorption lines with the Atacama Large Millimeter Array (ALMA) over a time span of six months in 2016. The monitoring is complemented by ALMA archival data in the 2012–2022 period. Observations are presented in Sect. 2. Section 3 covers the quasar continuum variations. Results from spectral line absorptions are given in Sect. 4. A discussion in Sect. 5 brings together the outcomes of continuum and spectral-line variations. A summary is given in Sect. 6.

2. Observations

2.1. 2016 monitoring campaign

Observations were made during ALMA Cycle 3, between March and September 2016. The proposed monitoring strategy comprised one visit every 10 days, over a time span of six months. To accommodate dynamic scheduling constraints, a time window of ± 7 days was set for each visit. A journal of the observations is given in Table 1. The proposed cadence was achieved – despite the scheduling challenge –, with a total of 17 successful visits. Among them, two visits were carried out on the same day (on 26 March 2016), providing a high signal-to-noise-ratio reference spectrum when combined, and the last visit (on September 8 2016) was carried out after a gap of 42 days with respect to the penultimate visit. Otherwise, the time intervals between visits range between 6 and 21 days.

During the monitoring, the array configuration changed, but the longest baseline was always longer than 450 m, such that the synthesized beam was always smaller than $0.5''$ and the two main lensed images of the quasar are therefore always well resolved. The on-source integration time for each visit was slightly less than 10 min, set by our original goal, which is to be able to track changes in the spectral line profiles down to a few percent during each individual visit.

Observations were made in dual polarization mode, with two orthogonal polarizers (XX and YY) in the antenna alt-azimuthal frame. The correlator setup was chosen to simultaneously cover the ground-state transitions of H_2O (557 GHz, rest frequency) and CH (two Λ -doublets at ~ 533 and 537 GHz, rest frequency) redshifted into Band 7. To cover these lines, three spectral windows were centered at ~ 282.4 , 284.6, and 295.4 GHz sky frequency, with a bandwidth of 938 MHz and a spectral resolution

Table 1. Journal of the 2016 ALMA monitoring and continuum data.

Date	MJD ^(a) (−50000)	N_{ant} ^(b)	PWV ^(c) (mm)	Flux calibrator	PA ^(d) (deg)	f_{NE} ^(e) (Jy)	f_{SW} ^(e) (Jy)	\mathcal{R} ^(f)	\mathcal{R}_{pol} ^(g) ($\times 10^{-3}$)	$\Delta\alpha$ ^(h)	σ ⁽ⁱ⁾ (%)
2016/03/05	7452.545	36	1.2	Titan	101	1.17	1.06	1.100 (3)	44.3 ± 1.3	0.146 (7)	0.49
2016/03/26	7473.385	42	1.0	J 1924–292	261	0.88	0.85	1.029 (1)	-12.5 ± 0.6	0.027 (7)	0.49
2016/03/26	7473.411	42	1.0	J 1924–292	259	0.91	0.89	1.025 (1)	-14.7 ± 0.7	0.032 (7)	0.47
2016/04/03	7481.398	43	1.9	J 1924–292	258	0.82	0.78	1.052 (1)	-29.8 ± 0.1	0.042 (9)	0.59
2016/04/10	7488.438	40	0.8	Titan	103	0.80	0.78	1.027 (1)	15.5 ± 1.1	0.039 (8)	0.49
2016/04/16	7494.526	37	0.9	Pallas	102	0.84	0.84	1.004 (1)	21.9 ± 0.8	0.017 (10)	0.73
2016/04/23	7501.262	40	0.8	Titan	260	0.71	0.73	0.967 (1)	3.9 ± 0.4	0.046 (9)	0.57
2016/05/02	7510.258	39	0.8	Titan	260	0.71	0.69	1.021 (1)	20.6 ± 0.4	0.073 (10)	0.64
2016/05/08	7516.430	41	1.5	Pallas	100	0.68	0.61	1.109 (1)	50.5 ± 0.4	0.072 (11)	0.77
2016/05/17	7525.258	41	1.3	J 1924–292	260	0.64	0.55	1.146 (1)	44.4 ± 0.4	0.065 (10)	0.64
2016/06/02	7541.442	37	1.3	Pallas	105	0.57	0.54	1.053 (1)	-0.4 ± 1.5	0.069 (28)	2.14
2016/06/15	7554.163	38	0.6	J 1924–292	261	0.64	0.67	0.963 (1)	-35.5 ± 0.4	-0.007 (10)	0.67
2016/06/22	7561.158	37	1.2	J 1924–292	260	0.61	0.58	1.044 (1)	-30.5 ± 0.5	0.000 (12)	0.95
2016/07/01	7570.236	42	1.1	J 1733–130	100	0.56	0.50	1.110 (1)	-10.9 ± 0.5	0.061 (12)	0.83
2016/07/14	7583.318	39	0.7	Pallas	104	0.56	0.50	1.115 (1)	1.7 ± 0.2	0.059 (15)	0.99
2016/07/28	7597.153	45	0.8	J 1733–130	100	0.43	0.45	0.962 (1)	0.6 ± 4.1	-0.031 (9)	0.68
2016/09/08	7639.162	39	0.6	J 1924–292	104	0.19	0.19	1.010 (2)	2.9 ± 0.6	0.111 (21)	1.16

Notes. ^(a)Modified Julian day; ^(b)Number of 12 m antennas in the array; ^(c)Average precipitable water vapor in the atmosphere during the observations; ^(d)Parallactic angle; ^(e)Flux densities of the NE and SW images, respectively. We adopt a conservative absolute flux accuracy of $\sim 20\%$; ^(f)Flux-density ratio between the NE and SW images, the number in parenthesis gives the uncertainty on the last digit; ^(g)Polarization ratio, as defined in Eq. (2); ^(h)Spectral index difference between the NE and SW images: $\Delta\alpha = \alpha_{\text{NE}} - \alpha_{\text{SW}}$; ⁽ⁱ⁾rms noise level of the spectrum between 295.0 and 295.4 GHz (i.e., a line-free region in the spectral window centered on the redshifted H_2O transition), in % of the continuum level of the SW image, at the native spectral resolution of $\sim 0.6 \text{ km s}^{-1}$.

Table 2. Complementary ALMA observations of H_2O , CH, and of the rare water isotopologs, H_2^{18}O and H_2^{17}O .

Species	Date	MJD ^(a) (−50000)	δv ^(b) (km s^{-1})	σ ^(c) (%)	f_{SW} ^(d) (Jy)
H_2O , CH	2012/04/11	6028.8	1.0	1.1	0.6
	2014/05/05	6782.8	0.5	1.3	0.3
	2014/07/19	6857.8	0.6	0.5	0.6
H_2^{18}O , H_2^{17}O	2014/05/05	6782.9	1.0	0.7	0.3
H_2^{18}O , H_2^{17}O	2014/07/18	6856.7	1.1	0.3	0.6
H_2^{18}O	2019/07/28	8692.1	1.1	0.1	1.7
H_2^{18}O , H_2^{17}O	2022/08/19	9810.0	1.1	0.2	0.8

Notes. ^(a)Modified Julian day; ^(b)Velocity resolution after Hanning smoothing; ^(c)rms sensitivity as a percentage of the SW image continuum level; ^(d)Flux density of the SW image.

of 0.56 MHz, resulting in a velocity resolution of 0.6 km s^{-1} after Hanning smoothing. A fourth spectral window, not including any detectable spectral line, was centered at 296.8 GHz with a coarser spectral resolution of 31.25 MHz in order to provide extra continuum data.

The calibration was done with the CASA (version 4.7.2) package (CASA Team 2022). The bandpass calibration was determined from the bright quasar J 1924–2914. The flux calibration was carried out using Titan (Butler-JPL-Horizons 2012 model), Pallas, J 1924–2914, or J 1733–130, as indicated in Table 1. We expect an absolute flux accuracy of the order of 10%–20% according to the ALMA Technical Handbook (Cortes et al. 2022). The gain calibrator was J 1832–2039 in all visits. After the standard calibration, a step of phase-only self-calibration on PKS 1830–211 was done with a short solution interval of 10 s.

The calibrated visibilities were finally fitted using the Python task UVMultiFit (Martí-Vidal et al. 2014) with a source model consisting of two point-like components, where the flux density of the NE image and the flux-density ratio, $\mathcal{R} = f_{\text{NE}}/f_{\text{SW}}$, were set as free parameters. Different fit runs were carried out using Stokes I data and data from the XX and YY polarizers separately in order to extract differential polarimetric information (see Sect. 3.4). The additional weak features of PKS 1830–211 reported from ALMA observations by Muller et al. (2020a), namely the third image (about 150 times weaker than the NE and SW images) and the small extensions from the NE and SW images (corresponding to the start of the Einstein ring and with a steep spectral index), have a negligible impact on the fitting process and were therefore not considered.

2.2. Complementary data

In addition to the 2016 monitoring data, we also used observations of PKS 1830–211 available in the ALMA archive to extract continuum information (flux density and flux density ratio) between 2012 and 2022, as well as previous ALMA observations of the same fundamental transitions of CH and H_2O as mentioned above, as well as of the rare isotopologs H_2^{18}O and H_2^{17}O (see Table 2). The data reduction was done with the same method as described above. All the spectral line data have a velocity resolution of $\sim 1.1 \text{ km s}^{-1}$ or better.

3. Results from continuum data

Table 1 lists the values of the flux densities, flux density ratios, polarization ratios, and spectral index differences of the two NE and SW lensed images during the 2016 monitoring and we present their time variations in Fig. 1. We used four

different flux-density calibrators (Titan, Pallas, J 1924–292, and J 1733–130). The data points follow a relatively smooth light curve, which is free of significant outliers, giving confidence that potential systematic effects in the flux calibration are limited. In addition, while the absolute flux accuracy is of $\sim 10\%$ – 20% , we emphasize that the accuracy of relative quantities, such as the flux-density ratio of both lensed images and the polarization ratio, is much higher (e.g., at a per mil level for the flux density ratio), and can therefore offer subtle diagnostics of the quasar activity, as discussed in the following subsections.

3.1. Submillimeter light curve

Over our six-month monitoring of PKS 1830–211, we observe a remarkable, nearly monotonic, and relatively featureless decrease in the flux density of the NE image, from ~ 1.2 Jy to ~ 0.2 Jy, which is a drop of more than 80% of its flux density at the start of the monitoring. The evolution of the NE and SW images is highly correlated and on a longer timescale than the time delay between the two images, indicating that this spectacular drop is intrinsic to the quasar and not due to a differential lensing effect. On average, the flux density decreased by ~ 5 mJy day $^{-1}$ over the six-month monitoring. This rate is small compared to previously reported flux variations of up to $\sim 10\%$ on an hourly timescale (e.g., Martí-Vidal et al. 2016; Martí-Vidal & Muller 2019), but it is remarkable that it was sustained over such a relatively long period.

3.2. Flux-density ratio

In contrast to the large decrease in flux density during the 2016 monitoring, the instantaneous flux-density ratios $\mathcal{R} = f_{\text{NE}}/f_{\text{SW}}$ show only mild ($\sim 10\%$) variations around an average value of ~ 1.04 , with extreme values of 0.96 and 1.15 (Fig. 1b). The flux-density ratio measurements, being relative by nature, are free from instrumental effects. Given the high signal-to-noise ratio of the data, their accuracy is of the order of one per mil. As discussed by Martí-Vidal et al. (2013), the variations of the flux-density ratio over timescales of shorter than a few days to a few weeks are likely a direct signature of the intrinsic activity of the quasar modulated by the time delay between the two images, because we would expect timescales of longer than a month for milli-lensing.

The flux-density ratio is best measured at mm/submm wavelengths, where the contribution from the Einstein ring is lower due to its steep spectral index (Jauncey et al. 1991, see also Muller et al. 2020a). However, prior to ALMA it was difficult to obtain mm observations with sufficient angular resolution to separate the two lensed images (partly due to the southern declination of PKS 1830–211 and to the small number of antennas of the previous generation of mm interferometers). Nevertheless, the flux-density ratio could be estimated from the saturation level of saturated lines, such as HCO $^+$ or HCN $J = 2-1$, which block the SW image almost completely (e.g., Wiklind & Combes 2001; Muller & Guélin 2008). Between 1995 and 2007, the flux-density ratio was found to vary between 1 and 3, but with only rare excursions to the extreme values. The average value of these old measurements was 1.7 ± 0.3 (Muller & Guélin 2008).

The flux-density ratios during the 2016 monitoring are among the lowest of all ALMA measurements since 2012, as shown in Fig. 2a. In 2012, the first ALMA Cycle 0 observations were taken serendipitously at the time of a γ -ray flare. The submm flux-density ratios showed remarkable temporal and chromatic variations between 1.2 and 1.5 within two months,

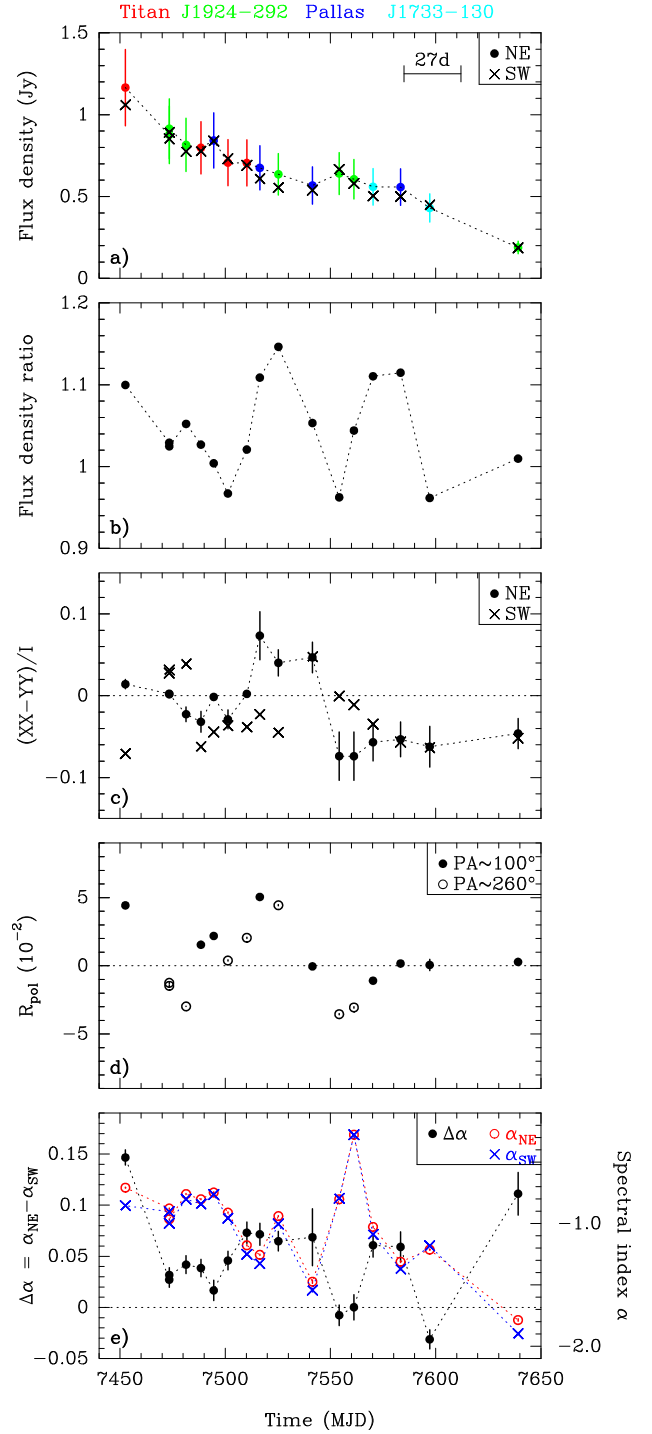


Fig. 1. Time evolution of the continuum properties of PKS 1830–211 during our monitoring in 2016 (see Table 1): (a) Flux density of the NE and SW images (error bars of 20% are indicated for the NE image data points only; the color code indicates the source used for flux density calibration). (b) NE/SW flux density ratio. (c) Difference in flux density between the XX and YY polarizers normalized by the Stokes I flux density. (d) Polarization ratio \mathcal{R}_{pol} (values are encoded as a function of the PA of the observations). (e) Difference in spectral index. The expected time delay of ~ 27 days between the two lensed images of the quasar is indicated in panel a.

which were interpreted by Martí-Vidal et al. (2013) with a simple model of plasmon injection and opacity effects in the jet of the quasar. Subsequent ALMA observations in 2014–2015 show

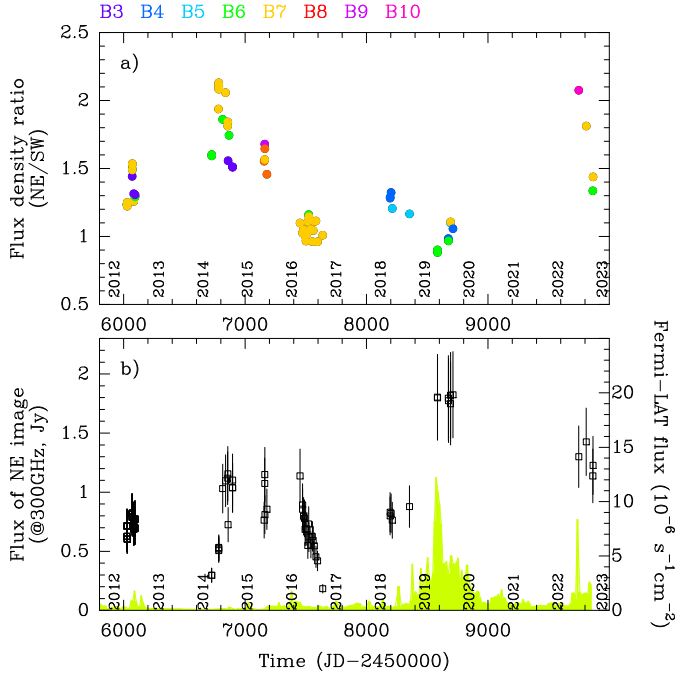


Fig. 2. History of ALMA measurements toward PKS 1830–211. (a) Flux-density ratios of PKS 1830–211 NE and SW images (with the color code corresponding to ALMA bands, as indicated at the top of the figure). (b) Flux densities of the NE image of PKS 1830–211, scaled to an equivalent frequency of 300 GHz such as $S_{300 \text{ GHz}} = S_\nu \times (\nu/300 \text{ GHz})^\alpha$ with a spectral index $\alpha = -0.7$ (error bars indicate a nominal flux uncertainty of 20%) overlaid on top of the *Fermi*-LAT γ -ray daily-monitoring light curve (in green).

slightly higher flux-density ratios between 1.4 and 2.2, contrasting with the measurements in 2016–2020, which are closer to ~ 1 , in particular those taken close in time to the record-breaking γ - and radio flare in 2019. The most recent measurements at hand (2022) show values in the range 1.3–2.0.

With the current collection of flux-density ratio measurements, it is difficult to obtain a clear and definitive determination of the true differential magnification, \mathcal{R}_q , between the two lensed images. Taken at face value, the average value of all the ALMA flux-density ratios measured between 2012 and 2022 is 1.38 ± 0.35 (with 1σ dispersion) and the median is 1.29. However, the evolution of the flux-density ratios in Fig. 2a shows a modulation on timescales of the order of several years, which could be the signature of “milli-lensing” (e.g., as discussed by Martí-Vidal et al. 2013). On shorter timescales of a few days to weeks, micro-lensing could also affect the picture (e.g., Wambsganss 1992). This could be tested with a long and regular time monitoring, including multifrequency observations in order to probe the chromaticity of the flux-density ratio evolution.

3.3. The time delay and the differential magnification factor

The determination of the geometrical time delay between lensed images is interesting for measuring the Hubble constant, H_0 , via the time-delay cosmography method (Refsdal 1964). Now that the third lensed image of the quasar has been unambiguously detected by Muller et al. (2020a) – thereby pinpointing the location of the lensing galaxy –, the major remaining sources of uncertainty for the lens modeling of the PKS 1830–211 system

that can be constrained observationally are the time delay and the relative magnification factor between the NE and SW images.

Both quantities have been investigated with different methods and at different wavelengths (see Table 3). At low radio frequencies, the required angular resolution of $<1''$ and the contamination from the Einstein ring make it difficult to disentangle the individual light curves from both images (van Ommen et al. 1995; Lovell et al. 1998). As mentioned above, it is possible to measure the flux-density ratio at mm wavelengths using the foreground molecular absorption and the saturation level of high-opacity lines, where absorption almost completely masks the SW image and therefore makes it possible to retrieve the flux densities of both NE and SW images even with low-angular-resolution data (Wiklind & Combes 2001; Muller et al. 2006). Time-series analyses of the γ -ray light curve benefit from long time ranges and daily monitoring¹. However, results with this method are still controversial (e.g., Barnacka et al. 2011; Abdo et al. 2015). Their interpretation might even be more complicated if individual γ -flares arise at different locations (Barnacka et al. 2015), implying slightly different time delays and magnification ratios. Overall, the results seem to converge toward a time delay in the range of 20–30 days and a differential magnification of ~ 1.0 – 1.5 , which seems consistent with a reasonable lens model (Muller et al. 2020a).

The relatively featureless light curve during our ALMA 2016 monitoring and potential effects from milli- or micro-lensing prevent us from setting new strong constraints on the time delay and differential magnification of the PKS 1830–211 system. Nonetheless, we applied a measure-of-randomness analysis (see, e.g., Chelouche et al. 2017) using the Von Neumann estimator (\mathcal{E}_{VN}), which is defined as:

$$\mathcal{E}_{VN}(\Delta t, \mathcal{R}_q) = \frac{1}{N-1} \sum_{i=1}^{N-1} [\mathcal{F}(t_i) - \mathcal{F}(t_{i+1})]^2, \quad (1)$$

where the datapoints $\mathcal{F}(t_i)$ correspond to the $(t_i; f_i^{\text{NE}})$ flux-density measurements from the NE image augmented with the $(t_i - \Delta t; \mathcal{R}_q \times f_i^{\text{SW}})$ points corresponding to the flux-density measurements of the SW image shifted in time by the time delay, Δt , and scaled by the differential magnification, \mathcal{R}_q , that is, $\mathcal{F}(t_i) = f_{\text{NE}}(t_i; f_i^{\text{NE}}) \cup f_{\text{SW}}(t_i - \Delta t; \mathcal{R}_q \times f_i^{\text{SW}})$. By varying the two quantities Δt and \mathcal{R}_q , we can calculate the corresponding values of \mathcal{E}_{VN} . The assumption of minimum randomness (as in the χ^2 minimization) points to the most likely values of the two parameters \mathcal{R}_q and Δt . We show the results of this analysis in Fig. 3. Given the quasi-monotonic and relatively featureless light curve of PKS 1830–211 during our monitoring, there is a strong degeneracy between the two parameters. Without significant a priori information on the differential magnification, we cannot better constrain the time delay with only our 2016 flux-density measurements. In Sect. 3.6, we further present a simple parametric model of the continuum evolution during the monitoring, from which we extract best-fit values of the time delay, namely 25 ± 3 days, and of the differential magnification, 1.25 ± 0.04 , which fall in the valley of lowest Von Neumann randomness in Fig. 3.

3.4. Differential polarimetry

To continue our analysis of the continuum emission properties of PKS 1830–211 during our monitoring, we can also investigate

¹ PKS 1830–211 is monitored by the *Fermi*-LAT satellite on a daily basis: https://fermi.gsfc.nasa.gov/ssc/data/access/lat/msl_1c/

Table 3. Previous measurements of the time delay Δt and the differential magnification \mathcal{R}_q between the NE and SW lensed images.

Observations date	Method	Δt (days)	\mathcal{R}_q	Note
1990–1991	Light-curve of VLA data at 8.4 and 15 GHz	$44 \pm 9^{(a)}$	1.17–1.23	van Ommen et al. (1995)
1997–1998	Light-curve of ATCA 8.6 GHz data	26^{+5}_{-4}	1.52 ± 0.05	Lovell et al. (1998)
1996–1998	Saturation of the HCO ⁺ $J = 2-1$ line	24^{+5}_{-4}	–	Wiklind & Combes (2001)
1997 Jan.–Apr.	43 GHz VLBI observations ^(b)	–	1.13 ± 0.61	Jin et al. (2003)
2008–2010	γ -ray light curve from <i>Fermi</i> -LAT	$27 \pm 0.6^{(c)}$	–	Barnacka et al. (2011)
2012 Apr.–Jun.	Model of a chromatic jet to ALMA data	$27^{(d)}$	1.35	Martí-Vidal et al. (2013)
2008–2015	γ -ray light curve from <i>Fermi</i> -LAT	$23 \pm 0.5, 19.7 \pm 1.2^{(e)}$	n.c. ^(e)	Barnacka et al. (2015)
2008–2011	γ -ray light curve from <i>Fermi</i> -LAT	n.a. ^(e)	$>6^{(e)}$	Abdo et al. (2015)
2019 Jul.	Lensing model from ALMA observations	$26-29^{(f)}$	$1.07^{(d)}$	Muller et al. (2020a)
2016 Mar.–Sep.	ALMA monitoring	$25 \pm 3^{(g)}$	$1.24 \pm 0.04^{(g)}$	This work

Notes. ^(a)Most likely contaminated by contribution of the Einstein ring flux density; ^(b)From the determinant of the relative magnification matrix between the two vectors formed by the core-jet separation and offset between polarized and total-intensity emission for different epochs; ^(c)Disputed by Abdo et al. (2015), as signal in the time-series analysis could come from the Moon’s orbital motion; ^(d)Fixed; ^(e)Not constrained, if different γ -ray flares arise from different emitting locations, hence with potentially slightly different time delays and magnifications; ^(f)Depending on the adopted value of H_0 ; ^(g)Based on a parametric model of the continuum evolution (flux density and spectral index).

the evolution of its polarization state. Although the ALMA data were not taken in full polarization mode, we can use the data obtained separately from the two orthogonal polarizers, XX and YY , in the alt-azimuth frame of the antennas to retrieve some source polarization properties using a differential polarimetry analysis (see, e.g., Martí-Vidal et al. 2015, 2016; Martí-Vidal & Muller 2019). First, we can form the difference ratio $\Delta_{XY} = (S_{XX} - S_{YY})/S_I$, where S_i are the signal retrieved from the XX and YY polarizers, and I is the Stokes I total flux. We already see in Fig. 1c that a clear polarization signal is present in the data, as Δ_{XY} varies within $\pm 8\%$ during the monitoring.

Furthermore, we can determine the flux-density ratios \mathcal{R}_{XX} and \mathcal{R}_{YY} from the XX and YY polarizers separately, and form the double polarization ratio, \mathcal{R}_{pol} :

$$\mathcal{R}_{\text{pol}} = \frac{1}{2} \left(\frac{\mathcal{R}_{XX}}{\mathcal{R}_{YY}} - 1 \right), \quad (2)$$

as defined by Martí-Vidal et al. (2015). If the quasar is not polarized or if both lensed images have strictly the same polarization properties (polarization intensity and electric vector position angle, hereafter EVPA), then $\mathcal{R}_{\text{pol}} = 0$. However, if the two images have different polarization properties, which could be due to a faster polarization variability than the time delay, then \mathcal{R}_{pol} would be a nonzero quantity that would depend on the polarization intensity and EVPA angle differences between the two images as well as on the parallactic angle of the observations. With observations at different frequencies, it is furthermore possible to derive the Faraday rotation from \mathcal{R}_{pol} (see Martí-Vidal et al. 2015, 2016).

The variations of \mathcal{R}_{pol} encode information on the polarization variability of the quasar. In Fig. 1d, we see that $|\mathcal{R}_{\text{pol}}|$ varies significantly between 0% and $\sim 5\%$ during the first half of the monitoring, but relaxes to ~ 0 after MJD = 7580. This suggests that the EVPA stabilized for a longer time interval than the time delay, after which the second image also stabilized. We note that the quasar fractional polarization eventually reaches a level of $\sim 5\%$, as shown by the nearly constant Δ_{XY} after MJD = 7580. This value is comparable to other polarization measurements in 2015 (Band 9, Martí-Vidal & Muller 2019) and 2019 (Band 6, Martí-Vidal et al. 2020), although the polarization variability can be significant over a shorter timescale than the time delay (Martí-Vidal et al. 2020).

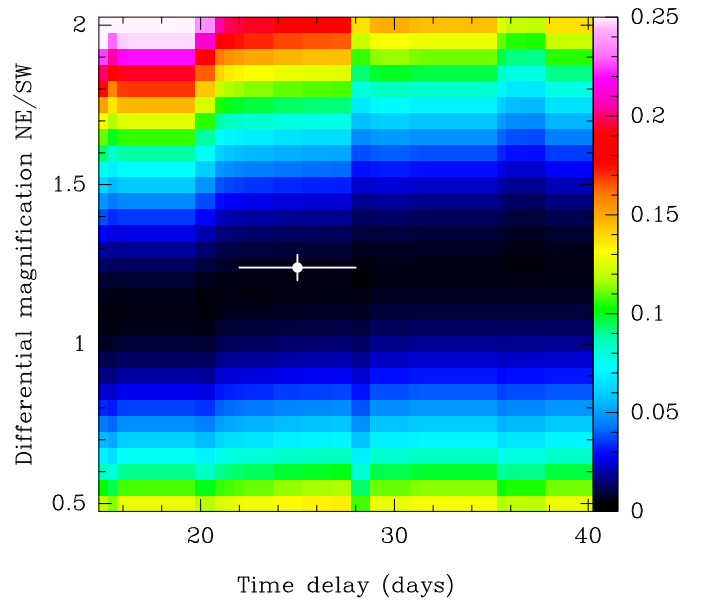


Fig. 3. Measure of randomness using the Von Neumann estimator \mathcal{E}_{VN} (defined in Eq. (1)) as a function of the time delay and differential magnification parameters. The best-fit value obtained from a parametric model of the continuum evolution (Sect. 3.6) is shown by the white mark.

3.5. Spectral index

We finally show in Fig. 1e the evolution of the spectral indices² of the two lensed images and their difference. The spectral indices were measured directly from the spectra corresponding to each lensed image after flagging channels associated with absorption features. We emphasize that any instrumental or calibration effects are removed when taking the spectral index difference $\Delta\alpha = \alpha_{\text{NE}} - \alpha_{\text{SW}}$ between the two lensed images.

Throughout the monitoring, the difference $\Delta\alpha$ was almost always positive, which reflects the rapid intrinsic variations of the quasar at a rate faster than the time delay, with the NE image having a steeper spectral index. Until the end of April 2016

² We define the spectral index α as $S(\nu) = S_0 \left(\frac{\nu}{\nu_0} \right)^\alpha$, $S(\nu)$ being the flux density as a function of the frequency.

(MJD ~ 7500), the spectral index is ~ -0.7 . It then gets a little steeper, except for a sudden rise of the quasar spectral index for two measurements around MJD = 7550 (15 and 22 June 2016), which corresponds to a small flux-density bump in the light curve.

It is interesting to note that the spread of $\Delta\alpha$ (i.e., between -0.05 and 0.15) in the different visits of our six-month monitoring is comparable to the change of $\Delta\alpha$ measured by Martí-Vidal et al. (2020) within a two-hour observation coincident in time with the onset of the 2019 record-breaking flare of PKS 1830–211. This suggests a considerable change of activity level between these two periods.

3.6. Simple scenario of the continuum evolution

The smooth and relatively slow flux-density evolution of the quasar suggests that the continuum spectra of the two lensed images should be similar, that is, that there are no clear features in the light curve on timescales short enough to introduce large differences between the NE and SW brightness or spectral index. Also, we do not consider the effects of micro- and milli-lensing here. If the decrease in source brightness was achromatic (i.e., if the flux density were to decay at the same rate for all frequencies), the spectral indices of the two images would be equal within the error bars. However, Fig. 1e shows that the spectral indices of the two images are systematically different at almost all epochs, the spectral index of the NE image being about ~ 0.05 higher than that of SW. One natural way to explain this difference in spectral index is to have a slower brightness decrease at higher frequencies, such that the leading NE image always has a slightly flatter spectrum than the SW image.

Here we propose a simple parametric model of the blazar continuum emission able to simultaneously explain the monotonic flux-density decay and the (small) difference in spectral index between the NE and SW images. The model assumes that the source brightness consists in two components: one that remains stable over time, that is, the core, and another that cools down adiabatically, that is, a moving feature, hereafter called a plasmon, injected in a conical jet. The total flux density in the time frame of the quasar $I(\nu, t)$ is then described as

$$I(\nu, t) \propto I_c + I_p \left(\frac{t}{t_0} \right)^\beta \left(\frac{\nu}{\nu_0} \right)^{\alpha_p}, \quad (3)$$

where I_c is the flux density of the core (assumed to have a flat spectrum), I_p is the flux density of the plasmon at $t = t_0$ and $\nu = \nu_0$, α_p is the spectral-index difference between the (optically thin) plasmon and the core, and β accounts for the brightness decrease due to the adiabatic expansion of the plasmon. For sake of simplicity, we do not consider radiative losses, but only adiabatic expansion, meaning that α_p remains constant over time (i.e., time and frequency dependencies are decoupled).

If the plasmon propagates downstream of a conical jet at a constant speed, the β index and I_p are related to the initial distance between the plasmon and the jet base, as well as to the propagation speed, because (for adiabatic losses) the energy of each synchrotron-emitting electron will decrease as (Pacholczyk 1970)

$$\dot{E} \propto \frac{E}{(r - r_0) \sin \theta} = \frac{E}{v \sin \theta (t - t_0)}, \quad (4)$$

where r and v are the distance (to the jet base) and the propagation speed, respectively, r_0 is the initial distance, and θ is the jet opening angle. Integrating this equation for an initial electron

population $N \propto E^{-p}$ (fixing $p = 3$) and computing the resulting synchrotron spectrum (with the assumption that $r \gg r_0$) results in $\beta = \frac{1}{v \sin \theta + k}$, where k depends on the choice of initial time, t_0 .

Using Eq. (3), we can estimate the spectral-index difference between the NE and SW images at any epoch:

$$\Delta\alpha(t) = \alpha_{\text{NE}} - \alpha_{\text{SW}}, \quad (5)$$

with

$$\alpha_{\text{NE}} = \frac{\log I(\nu_2, t) - \log I(\nu_1, t)}{\log \nu_2 - \log \nu_1}, \quad (6)$$

and

$$\alpha_{\text{SW}} = \frac{\log I(\nu_2, t - \Delta t) - \log I(\nu_1, t - \Delta t)}{\log \nu_2 - \log \nu_1}, \quad (7)$$

where Δt is the time delay between NE and SW images, ν_2 and ν_1 are the frequency pair used to compute the spectral index, and t is the time for the NE image. The time at the observer's frame, t' , would be stretched by the factor (which also affects Δt) given by

$$dt' = (1 + z) \frac{(v/c) \sin \delta}{1 - (v/c) \cos \delta} dt, \quad (8)$$

where z is the redshift of the quasar and δ is the angle between the jet and the line of sight. In our parametric model (Eq. (3)), the values of v , δ , and θ are all degenerated into β , I_0 , and the choice of t_0 . Hence, the time evolution of the model is only affected by β and Δt (in the observer's frame).

We show the results of this simple model simultaneously fitted to the light curve and spectral-index differences in Fig. 4. The corner plot results of a Markov chain Monte Carlo (MCMC) exploration of the plasmon injection time, I_c , I_p , β , α_p , the time delay, Δt , and the differential magnification are shown in Fig. 5. In this MCMC exploration, we have added a 10% systematic uncertainty to the flux densities and spectral indices, and have computed the error function using the flux densities of NE and SW images, the spectral index of NE, and the difference in spectral index between NE and SW. Even though the model is not able to reproduce the scatter seen in spectral index, it is remarkable that such a simple model can capture the light-curve decrease and the (overall) spectral differences between the NE and SW images in a consistent way. The values of the fitting parameters obtained from the MCMC exploration are given in Table 4.

The constraint on the time delay, Δt , is highly model dependent (i.e., the choice of the time evolution in Eq. (3)) and also changes if the relative weight between flux densities and spectral indices is changed in the error function. For instance, if the weight of the spectral index is increased or decreased by a factor 2, the value of Δt decreases or increases by ~ 3 or 7 days, respectively. The fitted value of Δt should therefore be taken with care. Still, the best fit value of $\Delta t = 25 \pm 3$ days is consistent with lensing models (Muller et al. 2020a). The differential magnification between the NE and SW images, on the other hand, is estimated to be 1.24 ± 0.04 and (together with the estimate of Δt) falls within the valley of lowest Von Neumann randomness shown in Fig. 3. The breaking of the time delay–differential magnification degeneracy that was noticed from the light-curve analysis is mainly due to the added information from the spectral index behavior, as Δt is also present in Eq. (7).

The main assumptions made for our modeling are as follows:

- We neglect effects from micro- and milli-lensing, and consider only intrinsic variations of the blazar.

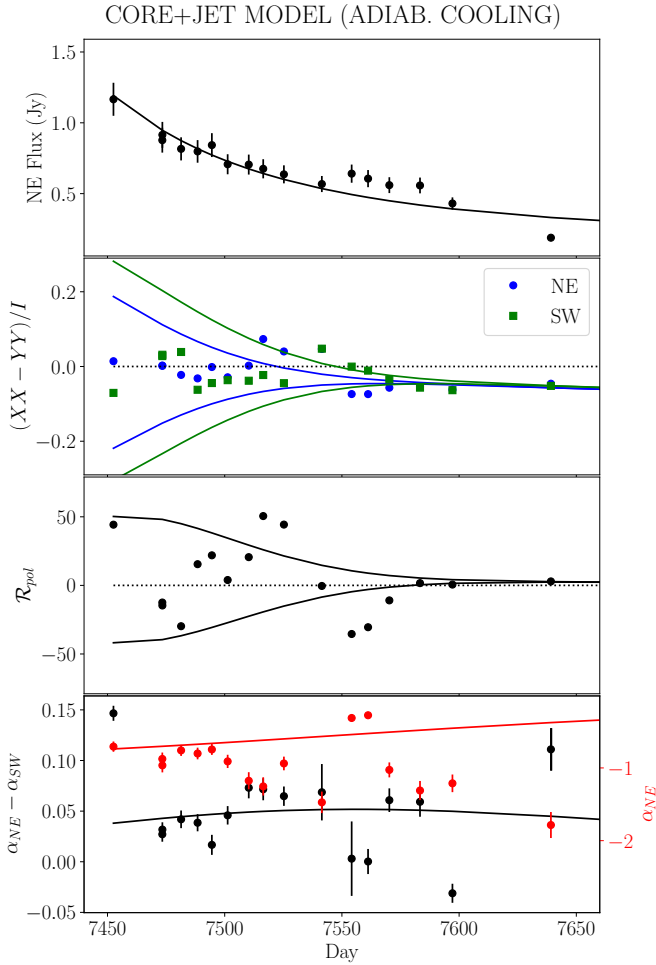


Fig. 4. Fit of the light curve, spectral index, and spectral-index difference between the NE and SW images using the parametric model provided by Eqs. (3) and (5). The envelope of extreme model values for the differential polarization quantities is plotted against measurements using the model extension described in Sect. 3.7. The fit also provides the spectral index of the NE image (red points).

- The emission from the core, I_c , is stable in time and is considered to be optically thick ($\alpha_c = 0$).
- A single event of plasmon injection.
- A straight trajectory of the plasmon (i.e., a ballistic plasmon), so that there are no changes in the Doppler boosting factor due to changes in the viewing angle.
- Radiative losses are negligible compared to adiabatic losses.
- We fix the jet orientation and opening angle (the actual values of these quantities are degenerated into the fitting parameters).
- The value of the core flux density is bound to be lower than the lowest flux density measured in the last epoch.

Our two-component model for the quasar continuum emission already provides a qualitative explanation for the evolution of the differential polarization, \mathcal{R}_{pol} . As the plasmon cools down as it propagates and expands in the jet, its contribution to the total flux density becomes smaller. Toward the end of our monitoring, the core (which would have a stable emission at timescales larger than the time delay) starts to dominate, and therefore produces similar polarization in the two images. Therefore, the differential polarization between the NE and SW images would vanish and \mathcal{R}_{pol} would tend to zero, as we indeed see in Fig. 1d.

3.7. Modeling with polarization evolution

We propose an extension to the model given in Eq. (3) to further account for the evolution of the polarization properties of PKS 1830–211 during the monitoring. The model starts with the same properties as described in the previous section, that is, a stable core and an evolving plasmon, and adds parameters for the polarization properties. We assume that the core fractional polarization, m_c , evolves slowly, that is, over a much longer timescale than the time delay, and is therefore taken as a constant in the model. On the other hand, we allow the fractional polarization of the plasmon, m_p , to vary in time. Accordingly, in addition to Eq. (3), we describe the evolution of the Stokes Q parameter (in the antenna frame) as:

$$Q = m_c I_c \cos(2\phi_c - 2\psi) + I_p \left(\frac{t}{t_0}\right)^\beta m_p F(t-t_0) \cos(2\phi_p - 2\psi), \quad (9)$$

where ψ is the parallactic angle, ϕ_c and ϕ_p are the core and plasmon EVPAs, respectively, and $F(t)$ is a function that must decrease quickly with time to match the observed behavior of \mathcal{R}_{pol} toward the end of the monitoring without increasing to very high values early on in the life of the plasmon. All the required model observable quantities (i.e., XX/YY and \mathcal{R}_{pol}) can then be computed from Stokes Q . By construction, the fit of the light curve (which uses total intensity) is decoupled from the polarization part, meaning that the parameters shown in Fig. 5 will not change from the effects of Eq. (9).

For the modeling of the data using Eq. (9), we notice that the parallactic angle coverage of our data is very limited, which prevents us from putting robust constraints on the core and plasmon EVPAs. Hence, we can only test the model of Eq. (9) and try to recover a qualitative behavior of our differential polarization measurements. For the sole purpose of a qualitative exploration, we set $F(t-t_0)$ to be Gaussian, with a width of 100 days, $m_c = 0.05$, and $m_p = 0.2$. The value of m_c is taken to be equal to $(XX - YY)/I$ toward the end of the monitoring, where we assume that the contribution from the plasmon polarization becomes negligible. The result of this model is shown in Fig. 4 (second and third panels). The lines shown are envelopes that account for every possible value of ϕ_c and ϕ_p , and assume that ϕ_c of the core is parallel to the parallactic angle in the last epochs of observation. From a qualitative point of view, the model recovers the basic behavior of converging toward a constant value of $(XX - YY)/I$ at late epochs (for both NE and SW), which in turn results in a null \mathcal{R}_{pol} at these epochs. Unfortunately, it is not possible to constrain the model further, as (besides the limited parallactic-angle coverage of our observations) the EVPA of the plasmon may be changing at a faster rate than our time sampling.

4. Results from spectral lines

The dramatic drop in flux density of PKS 1830–211 observed during our monitoring implies that there was substantial activity in the quasar, possibly with strong modifications of its continuum morphology. Only VLBI would be able to directly pinpoint such structural changes (see, e.g., Garrett et al. 1997). Nevertheless, time variations of the absorption line profile from the foreground absorber due to a varying continuum illumination can also provide some insight into the quasar’s activity and the absorbing screen properties.

Comparisons of a collection of $\text{HCO}^+ J = 2-1$ (Muller & Guélin 2008; Muller et al. 2014) and CS $J = 1-0$ (Schulz et al. 2015) absorption spectra have already revealed

Table 4. Best-fit values for the synchrotron-cooling ballistic plasmon model parameters (see Eq. (3) and Fig. 5).

	Parameter		Value	Note
Lensing	Time delay (days)	Δt	25 ± 3	Depends on plasmon model and data weights
	Differential magnification	\mathcal{R}_q	1.24 ± 0.04	Weakly coupled to Δt
Core	Flux density of the core (Jy)	I_c	0.178 ± 0.010	Bounded < 0.18 Jy
	Spectral index of the core	α_c	0	Fixed
Plasmon	Age of the plasmon at t_0 (days)		120 ± 30	Depends on plasmon model and data weights
	Flux density of the plasmon at t_0 (Jy)	I_p	1.51 ± 0.09	Weakly coupled to t_0
	Power of the plasmon flux-density decay	β	-2.2 ± 0.4	Strongly coupled to t_0
	Plasmon spectral index	α_p	-0.89 ± 0.02	

drastic changes over timescales of months and years. However, those observations were irregular and with consecutive visits spread over up to several months or even years.

Our dedicated 2016 monitoring with ALMA now allows us to track and investigate potentially subtle changes over a continuous six-month period and over timescales of down to ~ 10 days. We targeted the fundamental ground-state transitions of ortho- H_2O and CH (two Λ -doublets $J = 3/2-1/2$), which can be observed simultaneously in one ALMA tuning in band 7. Those lines were observed by ALMA in 2012 (Muller et al. 2014) and revisited in 2014 (Table 2). The H_2O absorption is deeply saturated toward the SW image near $v \sim 0 \text{ km s}^{-1}$ (Muller et al. 2014), but its large opacity is well suited to investigating the variations of the line wings. The H_2O line is also well suited to probing changes in the presumably optically thin NE absorption. On the other hand, the CH absorption reaches an apparent peak opacity of $\tau \sim 1$ along the SW line of sight, complementing the H_2O line in tracing variations in the line center of the SW absorption.

The collection of absorption spectra of the H_2O ground-state transition and of the two CH Λ -doublets is shown in Figs. B.1 and B.2 for each visit of our 2016 monitoring for the SW and NE lines of sight, respectively. The rms noise values for each visit –normalized to the continuum level– are given in Table 1 (last column) for the spectral window centered on the water line, which showed the lowest sensitivity. The two other spectral windows centered on the CH Λ -doublets show 10%–20% improved sensitivity. The lowest rms noise levels, of namely $\sim 0.5\%$ of the flux of the SW image (at the native channel resolution), were achieved at the start of the monitoring, when PKS 1830–211 had a high flux density. The rms noise increased to $\sim 1\%$ toward the end of the monitoring due to the quasar’s drop in flux density. Only for one visit (2 June 2016) was the noise level up to $\sim 2\%$ per channel due to poorer observing conditions. Hence, the ALMA monitoring provides us with the opportunity to trace variations of the absorption profile between two visits down to a level of about 1% of the continuum level, at a velocity resolution of $< 1 \text{ km s}^{-1}$.

4.1. Long-term variations (2012–2022)

Figure 6 shows all the available spectra of the H_2O (SW and NE lines of sight) and CH (SW line of sight only) lines taken with ALMA between 2012 and 2016 (observation details are listed in Tables 1 and 2). The spectra with large deviations with respect to the majority are highlighted with a special color code.

The main variations for the H_2O spectra toward the SW image do not occur in the line center near $v \sim 0 \text{ km s}^{-1}$, where the absorption is saturated, but in the wings of this component. The

blue wing (i.e., $v \sim -20$ to -60 km s^{-1}) appears to have been stable between the 2012 and 2014 spectra, but jumped to a new level between 2014 and 2016. In contrast, the red wing (i.e., $v \sim +20$ to $+60 \text{ km s}^{-1}$) shows more systematic variation, with the deepest absorption level being reached at the beginning of our survey in March 2016. This is not the case for the $v \sim +170 \text{ km s}^{-1}$ component, which was deepest in 2014 (Fig. 7). At the same time, the CH profile of the SW absorption does not show significant variation, except for some changes between 2012 and later observations.

Concerning the water absorption toward the NE image, there was a drastic decrease in the $v = -150 \text{ km s}^{-1}$ component between 2012 and 2014, whereas the subsequent spectra from 2014 to 2016 remain relatively unchanged. This major change is reminiscent of what happened between 2003 and 2006 in observations of the HCO^+ (2–1) line by Muller & Guélin (2008), with the near disappearance of the same velocity component during this time interval. For the $v = -225 \text{ km s}^{-1}$ feature, unnoticed prior to 2009 ATCA observations by Muller et al. (2011), the H_2O absorption varies continuously between 2012 and 2016 (Fig. 7). To these water spectra, we can add the observations of the CH^+ (1–0) line in 2015 (reported by Muller et al. 2017). If we scale down the optical depth of CH^+ by a factor of ~ 12 (see Fig. 8), its profile matches the $v = -150 \text{ km s}^{-1}$ feature relatively well, but is not consistent for the $v = -225 \text{ km s}^{-1}$ feature, suggesting that one or the other significantly varied again between 2015 and 2016.

Finally, there are a handful of observations of the rare water isotopologs H_2^{18}O and H_2^{17}O between 2014 and 2022 (Table 2 and shown in Fig. 9). Those reveal a spectacular increase in the H_2^{18}O absorption for the $v \sim -5 \text{ km s}^{-1}$ component in the July 2019 spectrum, when PKS 1830–211 was enduring a record-breaking γ - and radio flare (see Fig. 2b, and, e.g., Martí-Vidal et al. 2020). The integrated opacity of this component nearly increased by a factor four, while the absorption near $v = +5 \text{ km s}^{-1}$ did not change significantly. In particular, this remarkable change in absorption, together with the increase in the flux density of PKS 1830–211, allowed the detection of several deuterated species (Muller et al. 2020b). Interestingly, the most recent spectrum of H_2^{18}O obtained in August 2022 shows a return to almost the same profile as 2014, suggesting that the 2019 change was indeed due to an unusual event in PKS 1830–211, possibly related to a compact structure reminiscent of a typical Galactic dark cloud, as previously discussed by Muller et al. (2020b).

4.2. Time-variation statistics

The extremes of the 2016 H_2O and CH absorption spectra are shown in Fig. 10. The saturated region of the water absorption

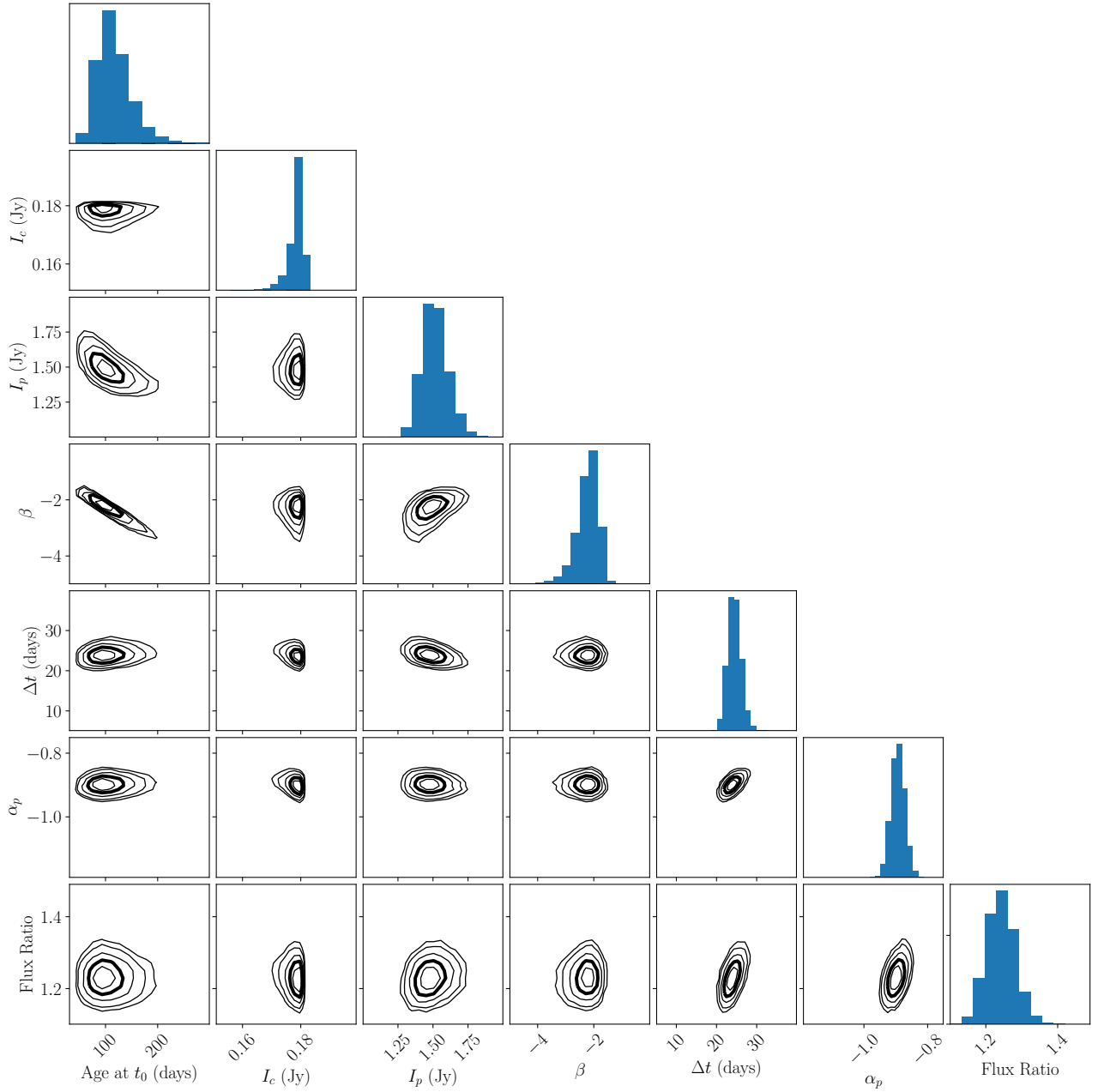


Fig. 5. Results from our plasmon modeling (Eq. (3)) as obtained from MCMC (see also Table 4).

toward the SW image ($v \sim 0 \text{ km s}^{-1}$ shows almost no variation, with the variation that we do see being due to a slight change of covering factor. It is interesting to note that the largest variations (up to $\sim 5\%$ of the continuum level) occurred in the line wings, especially in the red wing ($v \sim +40 \text{ km s}^{-1}$), but are not symmetric with respect to the line center. On the other hand, the variations seen in the CH spectra toward the SW image, of the $\text{H}_2\text{O } v \sim +170 \text{ km s}^{-1}$ component toward the SW image, and of the H_2O spectrum toward the NE image (i.e., all optically thin) are limited to an rms dispersion of $\lesssim 1\%$.

Furthermore, we show the difference between consecutive spectra divided by their respective time separation (i.e., rate of change) in Fig. 11. The strongest changes – which are of up to $\sim 1\%$ per day on average – appeared at the beginning of the monitoring. Nevertheless, variations are not restricted to single time events, but apparently occurred continuously during the monitoring.

4.3. Principal component analysis

To extract more information from the variations of the absorption line profile, we ran a principal component analysis (PCA). This method searches for maximum variance through the data and outputs the results in new orthogonal axes, that is, principal components (hereafter PCA eigenspectra) with their associated (eigen)values in order of decreasing variance. We used the `sklearn.decomposition.PCA` class in the scikit-learn Python package (Pedregosa et al. 2011) to retrieve the eigenspectra (i.e., as a function of velocity) and eigenvalues (i.e., as a function of time) of the monitoring spectra. The results of the PCA decomposition for the H_2O spectra toward the SW image are shown in Figs. 12 and 13 for the eigenvectors and eigenvalues, respectively. The three most significant PCA components consist in spectral features in the blue and red wings of the absorption profile, which resemble to some extent the difference spectra

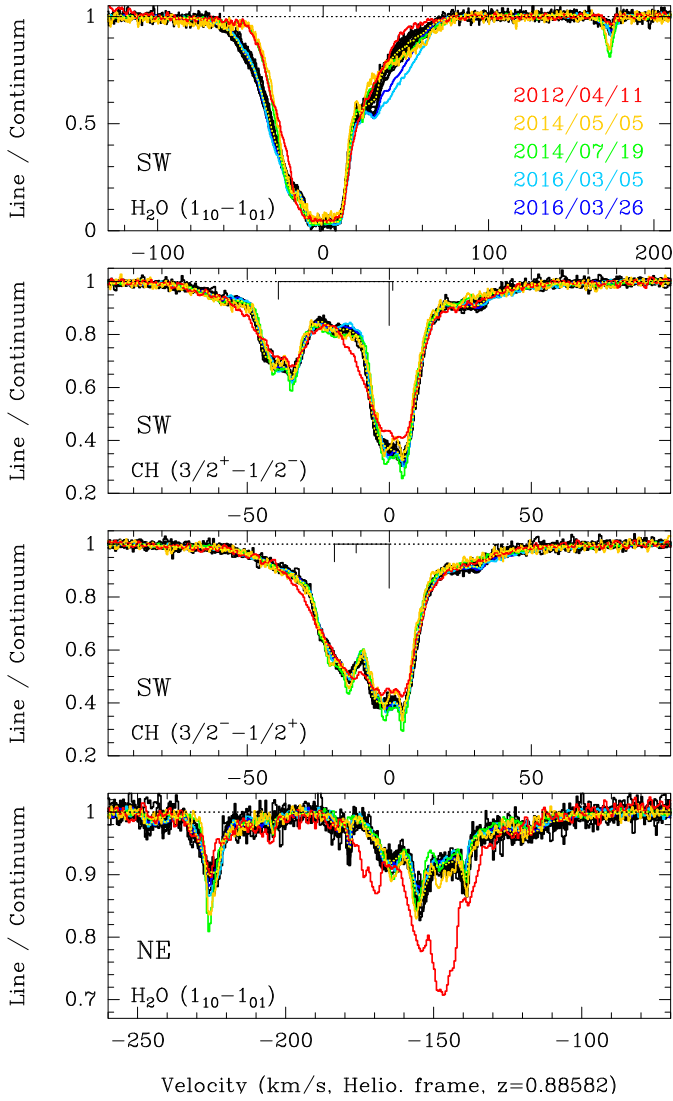


Fig. 6. Overlay of all ALMA spectra of H₂O (SW and NE lines of sight) and CH (SW only) observed toward PKS 1830–211 between 2012 and 2016. Special profiles showing clear deviations are highlighted with the color code given in the upper box.

shown in Fig. 11. Most interestingly, the evolution of the three first eigenvalues (all together describing more than half the variance of the data) does not appear to be random but can be well described by a sinusoidal function across the entire duration of the monitoring. Fitting such a sinusoidal function, we find periods of 272 ± 15 days, 186 ± 20 days, and 117 ± 12 days, for PC1, PC2, and PC3, respectively. These periods are comparable to the duration of our monitoring and it remains to be seen if the evolution is truly periodic with monitoring over longer timescales. Using the spectra of the CH doublets along the SW line of sight instead of H₂O, or the H₂O spectra along the NE line of sight, we also find apparent wavy behaviors for PC1, as shown in Fig. 14. In addition, we separately checked for the velocity intervals corresponding to the blue and red wings of the H₂O absorption along the SW line of sight, and, again, find wavy signals. A final test, taking a velocity range outside of any absorption features (i.e., purely noisy channels), shows no significant structure in the PCA decomposition. All these measurements (Table 5; except overlapping velocity range for measurements

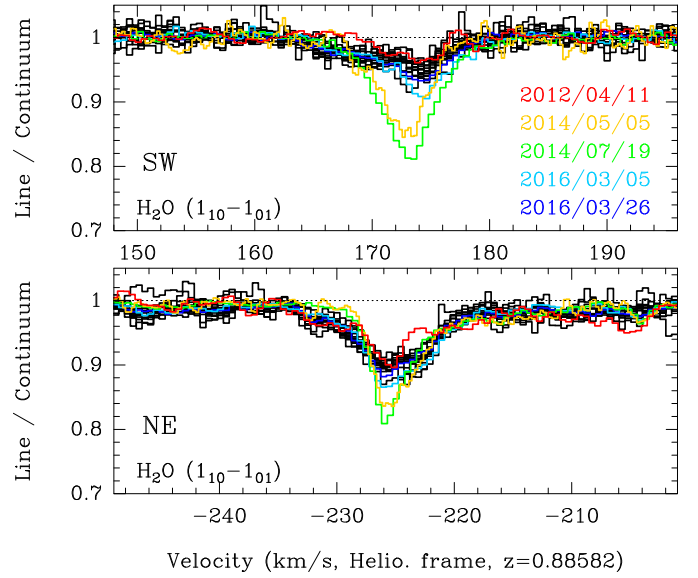


Fig. 7. Zoom onto the variations of the $+174 \text{ km s}^{-1}$ (top) and -225 km s^{-1} (bottom) features in the H₂O SW and NE spectra, respectively. Same as for Fig. 6; special profiles showing clear deviations are highlighted with the color code given in the upper box.

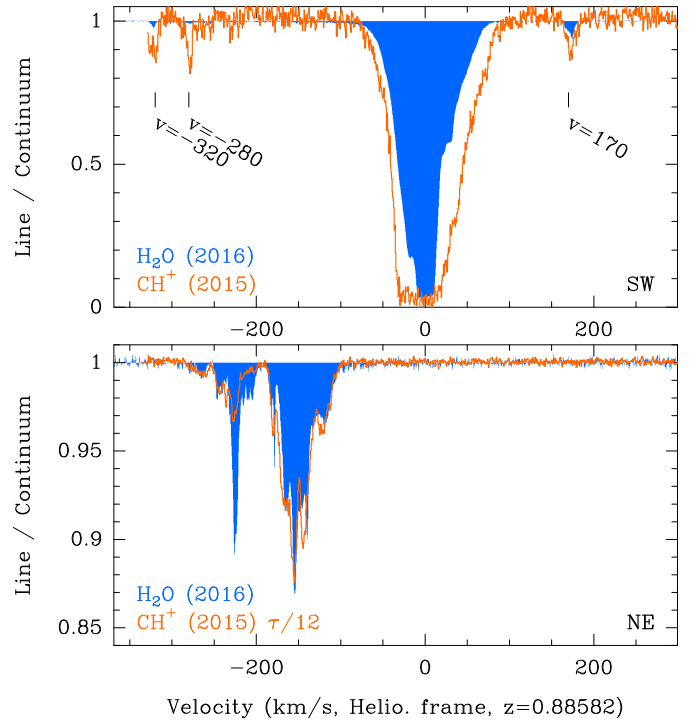


Fig. 8. Comparison of the average H₂O spectrum (filled blue) observed in 2016 with the ALMA CH⁺ (1–0) spectrum (orange line) observed in 2015 (Muller et al. 2017) for both lines of sight. For the NE spectrum, the opacity of the CH⁺ line, assuming a filling factor of unity, is reduced by a factor 12.

from H₂O spectra) are independent, but still yield a consistent signal period of ~ 230 days for PC1, within error bars.

In order to test the PCA performances, we ran experiments synthetic spectra with similar noise properties and time sampling as in the ALMA monitoring, in which we introduced a time varying component (with a given period) in the form of a Gaussian perturbation with a given amplitude, full width at half maximum

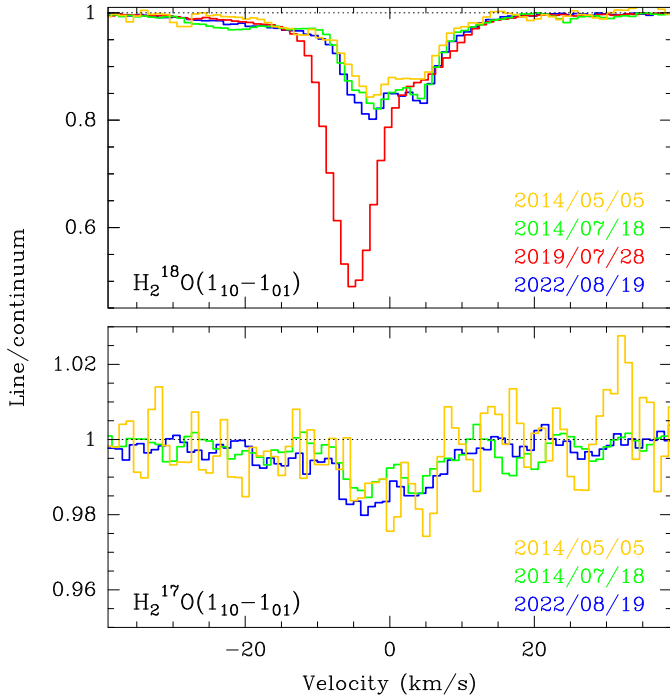


Fig. 9. Overlay of available ALMA spectra of H_2^{18}O and H_2^{17}O $1_{1,0} - 1_{0,1}$ toward the SW image of PKS 1830–211.

(FWHM), and velocity. We ran those synthetic spectra into the same PCA decomposition process as for the real observed spectra and the same fitting exercise with a sinusoidal function for the time evolution of the PC eigenvalues. We find that the first PC component PC1 succeeds in correctly retrieving (i.e., within error bars of the fit) the period for perturbation signals with S/N down to a few percent. In other words, the PCA, and particularly its PC1, shows a good performance in retrieving this signal.

As it is difficult to imagine any periodic behavior in the absorbing clouds simultaneously affecting both lines of sight and both H_2O and CH spectra, it is tempting to conclude that this wavy signal originates from the background illumination. This evolution could be connected to the model of a helical jet proposed by Nair et al. (2005), for which the precession period was estimated to be of one year. This interpretation would indeed bring a natural explanation for the time variability of the absorption lines toward PKS 1830–211, but would need to be tested with new monitoring data over a longer time span. In this scenario, we would observe a slow modulation of the absorption due to the jet helicity, with occasional bursts or dips of absorption, depending on whether or not there is favorable illumination, whenever a new plasmon or a local flare occurs in the jet.

4.4. 2016 averaged spectra

We take advantage of the multiple visits of the 2016 monitoring to produce deep average spectra of H_2O and CH absorptions toward both images. To achieve the best sensitivity and quality, we removed a spectral baseline as a first-order polynomial (i.e., corresponding to the intrinsic spectral index of each lensed image) on each individual spectrum. We then averaged all spectra after weighting them individually by the square invert of the rms noise levels listed in Table 1. The resulting high-sensitivity spectra have a noise level of better than 0.1%–0.2% of the normalized continuum level, as shown in Figs. 15 and 16. These “super” spectra lead us to two discoveries along the SW line

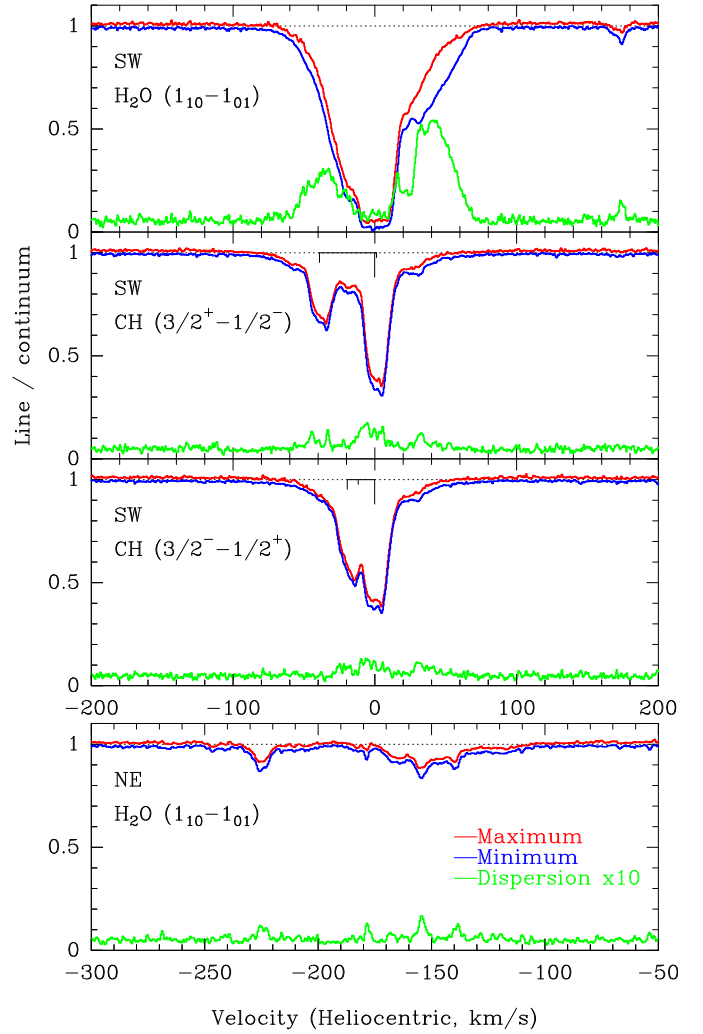


Fig. 10. Extrema and rms dispersion of the H_2O and CH absorption spectra during our 2016 monitoring (the CH profiles are not shown for the NE line of sight, because they contain only noise).

of sight: the detection of the weak absorption from the ^{13}CH isotopolog and a remarkable absorption trough of 500 km s^{-1} in width, both of which are discussed in the following subsections.

4.4.1. Detection of ^{13}CH

The rare isotopolog ^{13}CH was recently detected for the first time in the ISM of the Milky Way by Jacob et al. (2020). As CH is ubiquitous in the ISM, with optically thin lines, and is expected not to be affected by fractionation in its chemical formation, it appears to be an excellent species for measuring the $^{12}\text{C}/^{13}\text{C}$ elemental isotopic ratio (see a detailed discussion by Jacob et al. 2020). This isotopic ratio is an interesting probe of stellar nucleosynthesis history. Chemical-evolution models (e.g., Prantzos et al. 1996; Kobayashi et al. 2011) predict a positive $^{12}\text{C}/^{13}\text{C}$ gradient in the Milky Way, increasing with galactocentric distance and decreasing with time.

Here, we present the first detection of ^{13}CH toward the SW image of PKS 1830–211 in the average spectra of the 2016 monitoring data. The detection is robust, with its typical fine structure (see Table A.1) present in both Λ -doublets, as shown in Figs. 15a and b. Nevertheless, the ^{13}CH absorption signal is very weak, partly due to the optical thinness of CH, to the large $^{12}\text{C}/^{13}\text{C}$

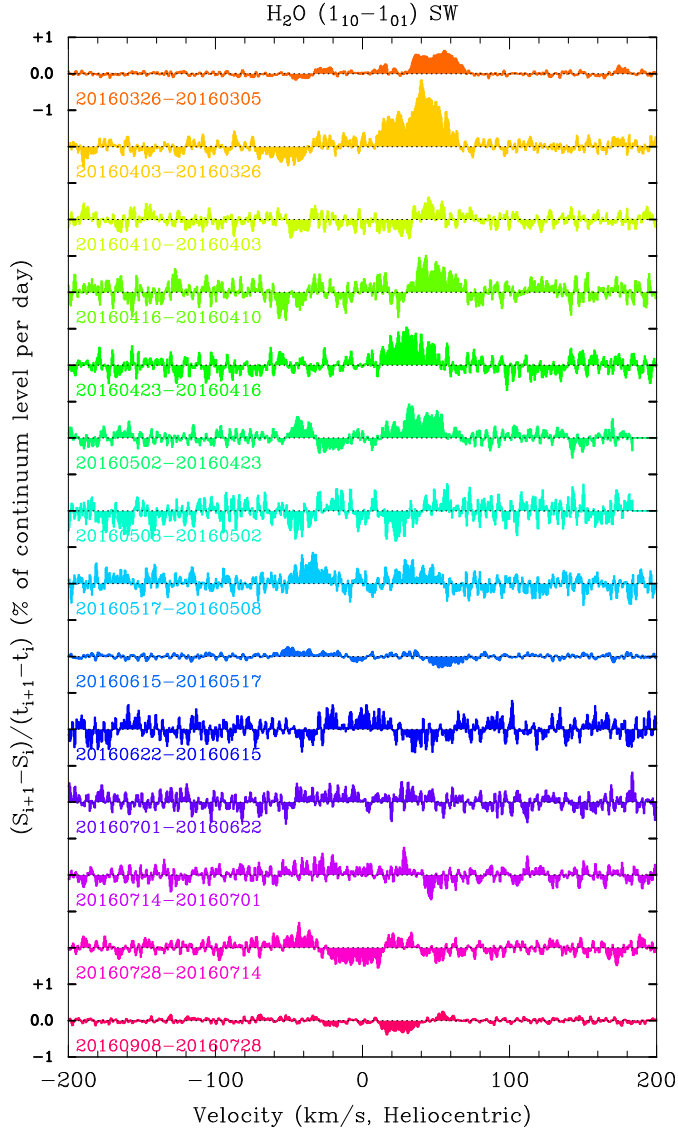


Fig. 11. Rate of the variations between consecutive observations of the H_2O absorption profile along the SW line of sight of PKS 1830-211.

isotopic ratio, and to the dilution of the signal among the many hyperfine components. We were able to obtain a detection in absorption toward PKS 1830-211 thanks to the brightness of the quasar and the high sensitivity of ALMA, providing a very high signal-to-noise ratio after averaging all the monitoring spectra.

In order to estimate the $^{12}\text{CH}/^{13}\text{CH}$ ratio, we performed a simultaneous fit of the two Λ -doublets of ^{12}CH and ^{13}CH for the SW absorption spectrum using the same intrinsic velocity profile for both CH and ^{13}CH convolved to their corresponding fine structure, respectively, and with the $^{12}\text{CH}/^{13}\text{CH}$ ratio as free scaling parameter. We made several attempts with increasing numbers of Gaussian velocity components to reproduce the absorption profile of CH, and obtained satisfying results using about ten components. During the process, we found that the ratio was relatively stable around approximately 150, while the uncertainties and fit residuals decrease with an increasing number of velocity components. Our final $^{12}\text{CH}/^{13}\text{CH}$ ratio is 150 ± 10 . The physical relevance of every single velocity component in the fit is not certain, but it is clear that a mix of narrow and broad components is needed to reproduce the profile, in par-

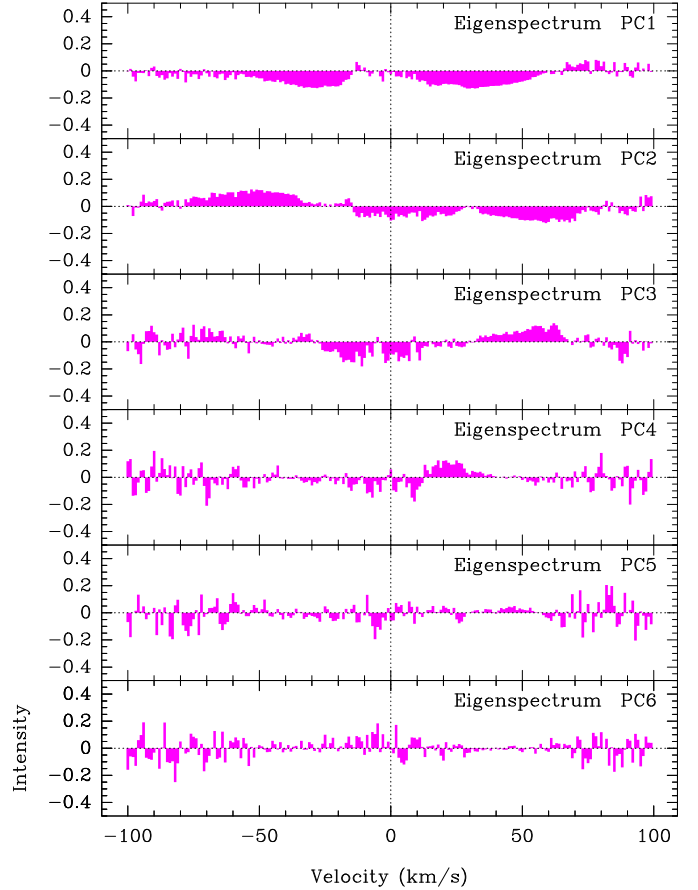


Fig. 12. Eigenspectra of the PCA decomposition of the H_2O spectra toward the SW image of PKS 1830-211.

ticular with some large components for the wings of the main $v = 0 \text{ km s}^{-1}$ absorption feature.

Compared to the $^{12}\text{C}/^{13}\text{C}$ - isotopolog ratios from other species in the SW line of sight toward PKS 1830-211, the $^{12}\text{CH}/^{13}\text{CH}$ ratio is the highest measured so far: 97 ± 6 for $^{12}\text{CH}^+ / ^{13}\text{CH}^+$ (Muller et al. 2017), 62 ± 3 for $\text{CH}_3\text{OH} / ^{13}\text{CH}_3\text{OH}$ (Muller et al. 2021), and even lower values 20 – 50 for HCO^+ , HCN, and HNC (Muller et al. 2006, 2011). This strongly suggests that all these other species may be affected by fractionation issues. A detailed analysis of the $^{12}\text{C}/^{13}\text{C}$ - isotopolog ratios is beyond the scope of this study and will be presented elsewhere.

A $^{12}\text{C}/^{13}\text{C}$ ratio ~ 150 in the $z = 0.89$ absorber is higher than the values observed within the inner 16 kpc of the Milky Way (see, e.g., the measurements of $^{12}\text{C}/^{13}\text{C}$ with galactocentric distance in Fig. 4 by Jacob et al. 2020); as such, it probably reflects a true evolution effect between the $z = 0.89$ absorber and the Milky Way today, as also found for other isotopic ratios (e.g., from N, O, S, Si, Muller et al. 2006, 2011).

4.4.2. Weak and broad water absorption trough in the SW sightline

In addition to the long-known main absorption features at $v \sim 0 \text{ km s}^{-1}$ and $v \sim -150 \text{ km s}^{-1}$ toward the SW and NE images, respectively (Wiklind & Combes 1998; Muller et al. 2006), Muller et al. (2011) discovered narrow velocity components at velocities of $v = -300, -224$, and $+170 \text{ km s}^{-1}$ in an unbiased 7 mm absorption survey with the Australian Telescope Compact Array. The -224 and $+170 \text{ km s}^{-1}$ components

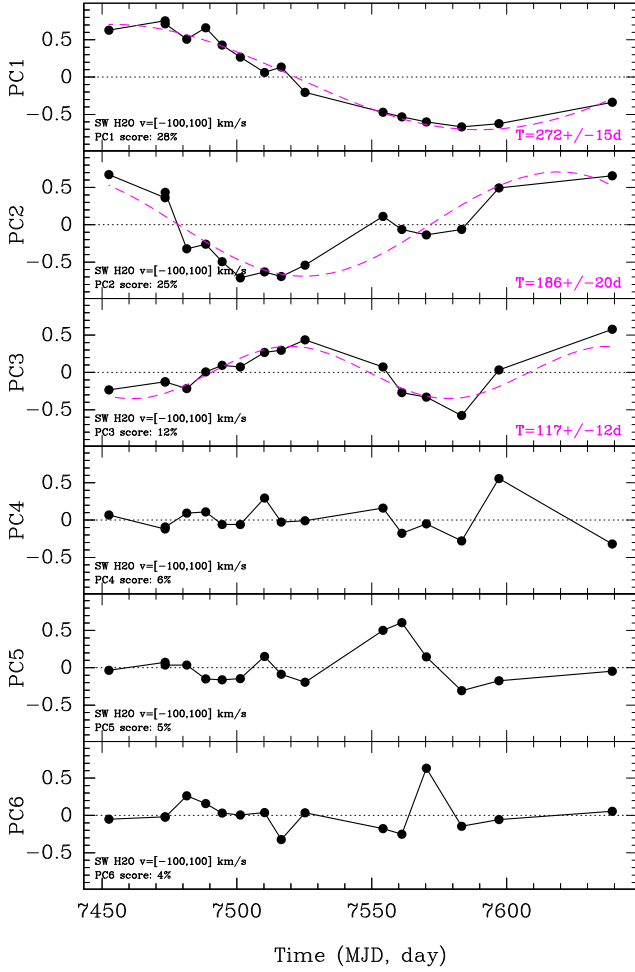


Fig. 13. Time evolution of the eigenvalues of the PCA decomposition of H₂O absorption spectra toward the SW image of PKS 1830–211.

Table 5. Fit results for different PCA runs.

Line of sight	Species	Velocity range (km s ⁻¹)	PC1 score (%)	T_{PC1} (days)
SW	H ₂ O	[-100, 100]	28	272 ± 15
		[-100, 0]	40	212 ± 11
		[0, 100]	44	228 ± 26
	CH1	[-60, 60]	34	270 ± 36
NE	CH2	[-60, 60]	26	266 ± 21
	H ₂ O	[-240, -120]	19	219 ± 15

Notes. The errors quoted for the period are those coming out of the fit of a sine function to the PC1 eigenvalues versus time, all eigenvalues taken with the same weight.

were later identified in ALMA data as occurring toward the NE and SW image, respectively (Muller et al. 2014), but the $v = -300$ km s⁻¹ component was not confirmed. However, two narrow velocity components at $v = -320$ and -280 km s⁻¹ were later observed in 2015 in the CH⁺ (1–0) ALMA spectrum toward the SW image (Fig. 8 and Muller et al. 2017), although near the edge of the spectral window. Both components are now readily confirmed in the H₂O “super” spectrum toward the SW image, as can be seen in Fig. 15c.

The origin of these components with large velocity spans in the line of sight is unclear, and they could be due to a high incli-

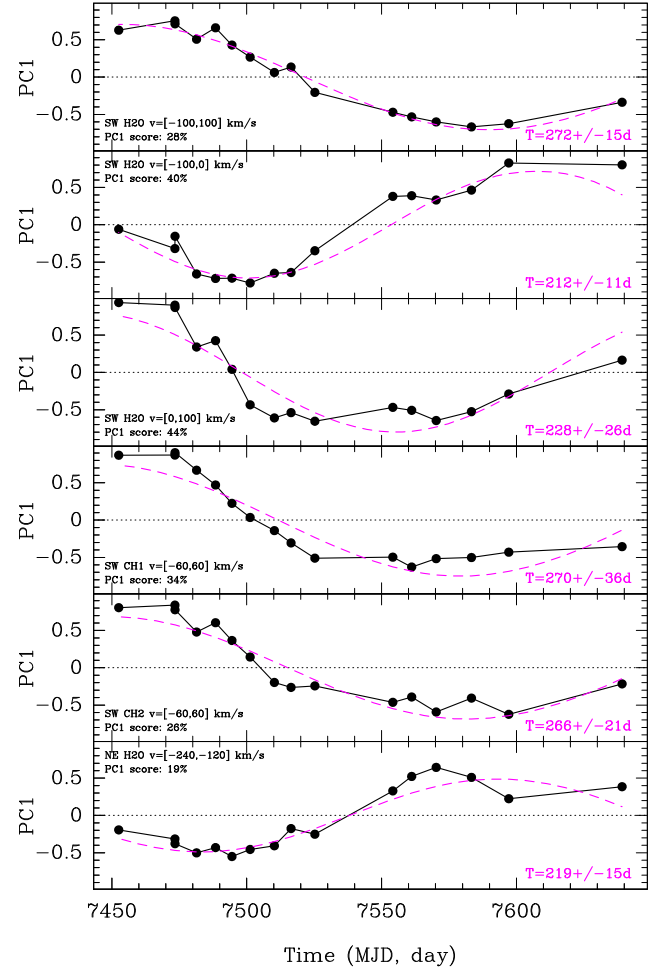


Fig. 14. Time evolution of the eigenvalues of the first component (PC1) of the PCA decomposition of various subsets of the monitoring spectra. The line of sight, species, considered velocity interval, and PC1 scores are given in each box.

nation of the absorber, large velocity gradients in the disk, or an extra-planar gas component, such as high-velocity clouds in the halo as observed around the Milky Way (as also discussed previously by Muller et al. 2014). They are not explained in the absorption kinematic model by Combes et al. (2021), which reproduces the HI and OH absorption spectra seen at cm wavelengths and the molecular absorption at mm wavelengths.

In addition, the ALMA “super” spectrum of the H₂O absorption now reveals an even more surprising structure in the form of a weak ($\tau < 0.01$) continuous absorption trough covering a wide velocity range of nearly 500 km s⁻¹ toward the SW image (Fig. 15c). This is much wider than the continuous absorption span of ~ 200 km s⁻¹ along the NE line of sight. It could be that this absorption trough reveals the presence of circumgalactic gas (e.g., Bahcall & Spitzer 1969; Tumlinson et al. 2017), although with up to such high velocities, it is not clear whether or not the gas would remain tied to the galaxy, depending on the halo-escape velocity, or would then (literally) form a “water fountain”. Given the lack of constraints on the distribution of such material in the halo (probably fragmented in filamentary structures), it is not possible to get a meaningful estimate of its mass content. In any case, we again emphasize the weakness of this signal, which would be extremely difficult to trace in

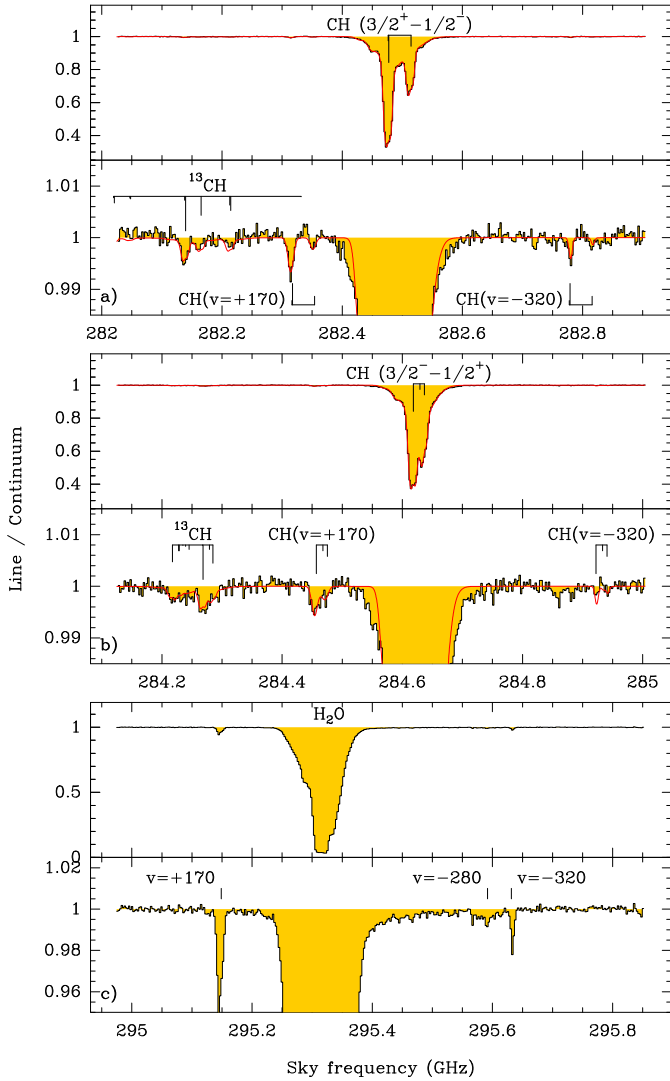


Fig. 15. Weighted-average spectra toward the SW image of PKS 1830–211, combining all visits in 2016. The hyperfine structure is shown for each CH Λ -doublet, with the strongest hfs component set at a velocity $v = 0 \text{ km s}^{-1}$, or as indicated otherwise. There are two boxes for each line, the first one showing the whole absorption spectrum and the second one showing a smaller range around the continuum level. Best-fit of the CH and ^{13}CH absorption is shown in red.

other galaxies unless a background continuum source as bright as PKS 1830–211 were present.

4.5. Water isotopologs and oxygen isotopic ratios

With different water isotopologs observed close in time in the 2014 and 2022 datasets (Table 2), we can derive the $\text{H}_2^{16}\text{O}:\text{H}_2^{18}\text{O}:\text{H}_2^{17}\text{O}$ isotopolog ratios of the water family. Those are not expected to be affected by fractionation effects and should therefore reflect the true elemental isotopic ratios of oxygen. For a given epoch, we assumed the same opacity profile (starting with five Gaussian velocity components) for all water isotopologs, as well as for CH when available in order to make the link between the high-opacity line of H_2^{16}O and the optically thin rare water isotopologs. We then fitted the opacity ratios as free scaling factors. When including the main water isotopolog, we also added the continuum-covering factor as a free parameter of the fit; otherwise, we fixed it to unity for the fit of the H_2^{18}O

and H_2^{17}O isotopologs alone. The results of our fitting exercises are summarized in Table 6. Due to the somewhat better signal-to-noise ratio of the data in July 2014, we used a higher number of Gaussian velocity components to obtain a better match of the profile and decrease the reduced χ -squared. However, we found that the fitted ratios were not drastically affected and remained similar within the uncertainties. The values of the $^{16}\text{O}/^{18}\text{O}$ ($=65.3 \pm 0.7$ after combining the measurements with their statistical weights) and $^{18}\text{O}/^{17}\text{O}$ ($=11.5 \pm 0.5$) ratios are consistent with the previous measurements made from the HCO^+ isotopologs by Muller et al. (2006, 2011), albeit with much better accuracy. Regarding the $^{12}\text{C}/^{13}\text{C}$ ratio discussed above (Sect. 4.4.1), the oxygen isotopic ratios point to a different ISM isotopic composition from that of the solar neighborhood in the Milky Way today (e.g., Lucas & Liszt 1998), namely one that is less processed and most likely dominated by massive-star nucleosynthesis (see also, e.g., Wallström et al. 2016; Martín et al. 2019; Tang et al. 2019 and references therein).

5. Discussion

5.1. Analysis of the absorption profiles and their time variations

The absorption spectrum S_ν resulting from an absorbing screen with opacity $\tau_\nu(x, y)$ (x and y being in the plane of the sky) in front of a background continuum illumination $i(x, y)$ and normalized to it is

$$S_\nu = \frac{1}{I_{\text{tot}}} \iint i(x, y) e^{-\tau_\nu(x, y)} dx dy, \quad (10)$$

where $I_{\text{tot}} = \iint i(x, y) dx dy$ is the total continuum intensity. Therefore, the normalized absorption spectrum is the continuum intensity-weighted average of the exponential of the opacity distribution of the illuminated material: $S = \langle e^{-\tau(x, y)} \rangle_i$. In the case where the continuum emission is spatially extended but unresolved by the observations, the distributions $i(x, y)$ and $\tau(x, y)$ are unknown, and we can only measure I_{tot} and the resulting normalized absorption spectrum S_ν . If we consider a representative average opacity $\langle \tau'_\nu \rangle$, Eq. (10) can be expressed as:

$$S_\nu = 1 - f_c \times (1 - e^{-\langle \tau'_\nu \rangle}), \quad (11)$$

where we introduce the source-covering factor f_c , which is defined as

$$f_c = \frac{\iint_{\Omega_{\text{abs}}} i(x, y) dx dy}{I_{\text{tot}}}, \quad (12)$$

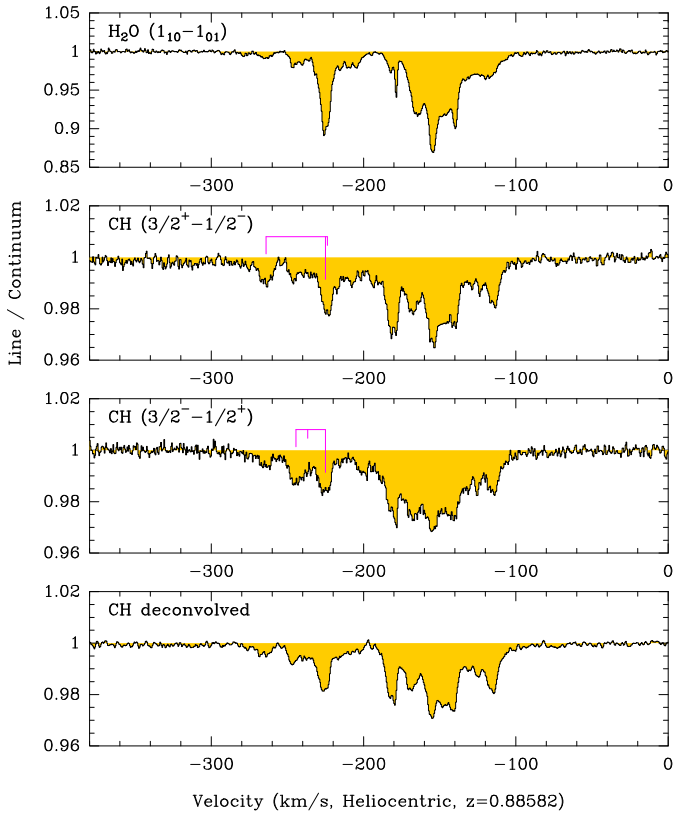
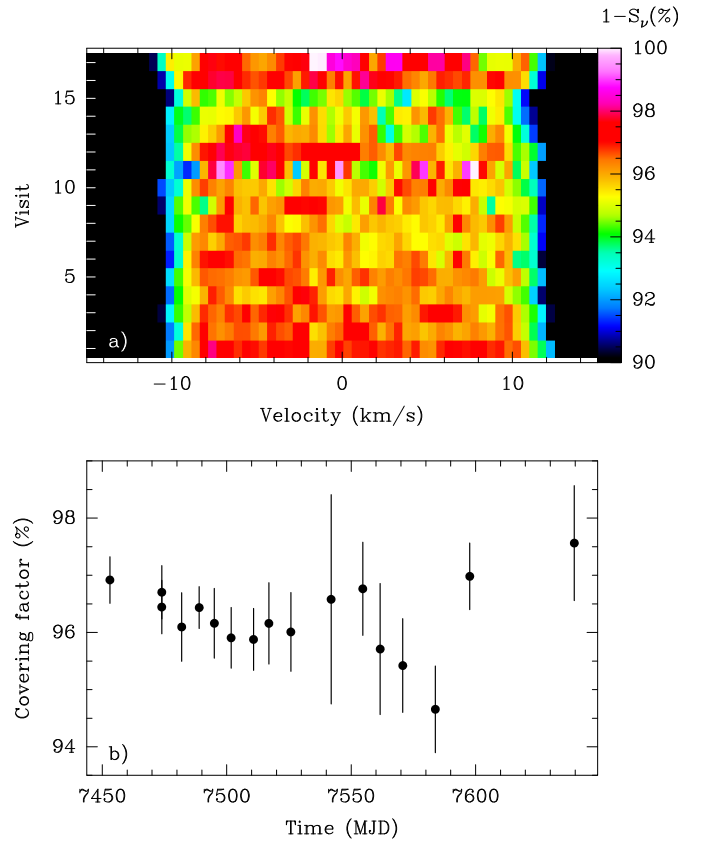
where Ω_{abs} is the solid angle fraction of the background continuum actually covered by absorbing material (weighted by intensity); by construction: $0 \leq f_c \leq 1$.

The most straightforward way to measure the covering factor is to use the saturated region of a very optically thick line, such as the $\text{H}_2\text{O } 1_{10} - 1_{01}$ in our case ($\tau \gtrsim 10$). Figure 17 shows the measurements of f_c across the different visits of our 2016 monitoring. The covering factor is $\sim 96\%$ with only mild variations of the order of 1%, which contrast with the large variations of the flux density between the beginning and the end of our monitoring (Fig. 1). The values of f_c are consistent with previous measurements of saturated lines (Muller et al. 2014).

To further characterize the absorption variations, we can assume that the absorbing screen is constant in time, that is, $d\tau(x, y)/dt = 0$. This is justified by the fact that the timescales

Table 6. Results for a global fit using the same opacity profile for different combinations of lines and epochs.

Species	Date	$N_{\text{gauss}}^{(a)}$	$f_c^{(b)}$	$\text{H}_2\text{O}/\text{CH}^{(c)}$	$\text{H}_2^{16}\text{O}/\text{H}_2^{18}\text{O}^{(c)}$	$\text{H}_2^{18}\text{O}/\text{H}_2^{17}\text{O}^{(c)}$	$\chi_r^2^{(d)}$
$\text{H}_2\text{O}, \text{H}_2^{18}\text{O}, \text{H}_2^{17}\text{O}, \text{CH}$	2014/05/05	5	0.942 (3)	8.6 ± 0.1	68.5 ± 1.4	9.4 ± 1.3	1.09
$\text{H}_2\text{O}, \text{H}_2^{18}\text{O}, \text{H}_2^{17}\text{O}, \text{CH}$	2014/07/18-19	5	0.975 (2)	9.18 ± 0.07	65.9 ± 1.0	14.0 ± 2.3	3.85
$\text{H}_2\text{O}, \text{H}_2^{18}\text{O}, \text{H}_2^{17}\text{O}, \text{CH}$	2014/07/18-19	9	0.975 (2)	8.90 ± 0.05	64.2 ± 0.8	14.1 ± 1.8	2.29
$\text{H}_2^{18}\text{O}, \text{H}_2^{17}\text{O}$	2014/05/05	3	1 ^(e)	—	—	9.6 ± 2.1	1.35
$\text{H}_2^{18}\text{O}, \text{H}_2^{17}\text{O}$	2014/07/18	3	1 ^(e)	—	—	13.9 ± 1.1	1.31
$\text{H}_2^{18}\text{O}, \text{H}_2^{17}\text{O}$	2022/08/19	3	1 ^(e)	—	—	11.0 ± 0.6	1.25

Notes. ^(a)Number of Gaussian components in the absorption profile; ^(b)Continuum filling factor; ^(c)Line opacity ratio (for CH, this refers to an hfs component of relative strength unity); ^(d)Reduced chi-squared; ^(e)Fixed.**Fig. 16.** Weighted-average spectra toward the NE image of PKS 1830–211, combining all visits in 2016. The hyperfine structure is shown for each CH Λ -doublet, with the strongest hfs component set at a velocity $v = -150 \text{ km s}^{-1}$. The lower panel shows the CH hfs-deconvolved profile.**Fig. 17.** Measurements of the covering factor across the different visits of our 2016 monitoring. (a) Saturation level ($1 - S_v$) at the center of the H_2O line for all the visits in 2016. (b) The values of all spectral channels with velocities $|v| < 8 \text{ km s}^{-1}$ are averaged to provide measurements of the continuum-covering factor as a function of time.

associated with potential causes of variations in the absorber are much longer than those we are interested in, even for small-scale structures on AU- to pc-scales. For example, a structure of 10 AU with a velocity of 200 km s^{-1} in the plane of the sky (e.g., due to rotation for a face-on spiral galaxy) would have a crossing time in front of a fixed point-like continuum of three months. For a cloud collapse, the free-fall timescale is $t_{\text{ff}} \sim 2 \text{ months} \sqrt{\frac{(R/\text{AU})^3}{(M/M_\odot)}}$, where R is the cloud size and M its mass. Finally, we can also exclude variations due to a change of the chemical composition of the absorbing material, because typical chemical timescales are orders of magnitude longer than years (e.g., Tielens 2005; Valdivia et al. 2017). Therefore, we need only consider time variations due to structural changes of the quasar’s morphology, that is, change of $i(x, y)$ with time.

If the absorbing screen is uniform, where $\tau(x, y) = \tau_0$, there can be no variation of the normalized absorption spectrum, regardless of variations of $i(x, y)$. Consequently, the mere observation of variations of the absorption spectra implies that there are opacity structures in the absorbing screen at scales smaller than the continuum size. Similarly, a simple change of $i(x, y)$ by a multiplicative factor would not induce variations of the absorption spectrum due to the normalization by I_{tot} , and therefore variations of S_v also imply small-scale structures in the quasar’s continuum emission. Hence, the absorption variations reflect the coupling of small-scale structures between the continuum $i(x, y)$ and absorbing screen $\tau(x, y)$.

Taking Eq. (11) as a simplified description of the absorption spectra and assuming that all continuum variations result in a change of the average opacity, then the derivative $dS_\nu/d\tau$ yields an estimate of the variation; we get

$$\Delta S \propto \tau e^{-\tau} \left(\frac{\Delta \tau}{\tau} \right). \quad (13)$$

The function $x e^{-x}$ peaks sharply for $x = 1$ and tends rapidly to zero for large x , explaining why the maximum variations of the water absorption are seen in the line wings but are strongly attenuated at the saturated line center.

5.1.1. Possible causes of time variations of the continuum distribution

In the long term (months to years), we have seen some drastic changes in the absorption profiles, such as the near disappearance of the NE absorption near -150 km s^{-1} between 2003 and 2006 (Muller & Guélin 2008), its drastic decrease between 2012 and 2014, or the doubling of the absorption depth for the $v = -5 \text{ km s}^{-1}$ velocity component in the H_2^{18}O SW profile observed in 2019 (Fig. 9 and Muller et al. 2021). This last event was occurring at the time of a record-breaking flare of PKS 1830–211 at γ -rays and radio. It is possible that one or another cloud becomes occasionally illuminated (or highlighted) by a new continuum component. This “occasional event” scenario is consistent with the fact that the last H_2^{18}O spectrum in 2022 shows that the absorption returned to almost the same profile as pre-2019, which we could then qualify as a “quiescent absorption profile”. Nevertheless, at this stage, we cannot exclude the possible effect of milli-lensing on timescales of months to years. In 2019, the flux-density ratio was indeed in the low range of values (i.e., either the NE image was fainter than usual with respect to the SW image, or the SW image was brighter than the NE image). We would need more statistics of drastic absorption-change events to investigate a possible connection with γ -ray and radio flares.

On shorter timescales of weeks to months, the effect of micro-lensing on the variability of absorption spectra was investigated by Lewis & Iбата (2003). The picture is highly complicated by the large parameter space defined by absorbing cloud properties (shape, size, absorption profile) and distribution with respect to the background continuum illumination (all unknown), but Lewis & Iбата (2003) validate the fact that micro-lensing can potentially induce significant modulation of the absorbing signal provided absorbing clouds have subparsec-scale structures.

An object of mass M in the lens plane can produce significant variability by (micro-)lensing for a typical source size below the Einstein radius:

$$\theta_E = \sqrt{\frac{4GM}{c^2} \frac{D_{ls}}{D_{ol}D_{os}}}, \quad (14)$$

where D_{ij} are the angular diameter distances between the observer o , the lens l , and the source s , respectively. For PKS 1830–211 and a stellar-mass object, $\theta_E \sim 2 \mu\text{as}$.

The size of the SW core was measured to be $\theta_{\text{SW}} \sim 0.1 \text{ mas}$ at $\lambda \sim 1 \text{ cm}$ and to scale with a $\sim \lambda^2$ dependence at radio–cm wavelengths (Guirado et al. 1999). Extrapolating this behavior to mm wavelengths, we would obtain a size of $1 \mu\text{as}$ at $\lambda \sim 1 \text{ mm}$. However, broadening due to interstellar scattering may have a far less significant effect at mm/submm wavelengths. In fact, Muller et al. (2021) estimated a flatter dependence in $\lambda^{0.3}$ from

the covering factors derived from a set of submm methanol lines. Extrapolating the size measurement at 1 cm with this flatter dependence, we obtain a size estimate of about $50 \mu\text{as}$ at 1 mm ³, which is roughly one order of magnitude larger than θ_E . Therefore, it is possible that micro-lensing induces variability on timescales of weeks to months, which corresponds to the caustic crossing time (Lewis & Iбата 2003).

On the other hand, the scenario of a helical jet would naturally induce variations of the continuum illumination with a clear periodicity. In turn, this periodicity may be imprinted in the variations of the absorption profile, which could be what we observe in the 2016 spectra, as suggested by our PC analysis (Sect. 4.3). In Sect. 3.6, we propose a simple parametric model of a single ballistic plasmon in the jet to account for the continuum evolution during the 2016 monitoring. The ballistic assumption would not necessarily be in contradiction with the helical jet scenario. The toy model would also work even if the plasmon path is helical within the jet and its opening angle. There could be a time-changing Doppler boosting that would be added to the power-law decay of the toy model (depending on how open the helical path is and how close the jet line is to the line of sight), but the effect could be hidden below the flux-density uncertainties. Moreover, the facts that (i) we see a clear sinusoidal signal in the PCA and that (ii) the largest variations of the absorption profile happened at the beginning of the monitoring may support the single plasmon injection event. Indeed, supposing there were more plasmons at different points of the helical jet, one would see a “dirty” superposition of sinusoids with different phases. Therefore, having one simple sinusoidal signal in the absorption variation may be telling us that the illumination pattern of the absorbing clouds was simple during the 2016 monitoring.

Given the quasi-monotonic and severe decrease in the flux density of PKS 1830–211 during our six-month monitoring (by $\sim 80\%$), the short (timescale of the order of one week) and regular variations of the absorption spectra, and the apparent coherence (periodicity?) of the variations over ≥ 200 days seen toward both lensed images, we conclude that they are most likely due to intrinsic changes in the background continuum distribution, that is, the activity of the quasar, rather than to micro-lensing events. Eventually, the different scenarios (helical jet or lensing-induced variations) could be tested with long-term (i.e., more than one year long) monitoring of the absorption variation and its potential periodicity (e.g., with ALMA) and continuum structural changes (e.g., with VLBI), although flaring or micro- and milli-lensing events could occasionally confuse a periodic signal induced by the jet helicity.

5.1.2. Variations on short timescales

We now consider variations on short timescales – that is, between two consecutive observations at t_1 and t_2 – resulting from intrinsic morphological changes in the blazar. Accordingly, we assume that the characteristic size scale, a causal region of size $c(t_2 - t_1)$, is small compared to the overall continuum emission.

We can then introduce the continuum distribution $i_2(x, y, t_2) = i_1(x, y, t_1) + \delta i(x, y)$, where $\delta i(x, y) = 0$ outside of the small region of the continuum that was indeed affected by changes between t_1 and t_2 . We do not need to assume any specific shape for this region, except that it is strictly included within a circle of radius $c(t_2 - t_1)$ or θ_E centered toward the direction x_c, y_c in the sky. We express the new normalized absorption spectrum S_2 from Eq. (10):

³ This corresponds to 0.4 pc in the $z = 0.89$ absorber.

$S_2 = \frac{1}{I_1 + \delta I} \iint (i_1(x, y) + \delta i(x, y)) e^{-\tau(x, y)} dx dy$. Rewriting the equation for $\delta I/I_1 \ll 1$, and neglecting the second-order terms in $\delta I/I_1$, we get:

$$\Delta S = S_2 - S_1 = \frac{1}{I_1} \iint \left(\delta i - \frac{\delta I}{I_1} i_1 \right) e^{-\tau} dx dy. \quad (15)$$

Furthermore, we assume that the absorbing material illuminated by the continuum region $\delta i(x, y)$ has homogeneous opacity $\tau_c = \tau(x_c, y_c)$. After simplifying the integral summation, we obtain:

$$\Delta S = \frac{\delta I}{I_1} (e^{-\tau_c} - \langle e^{-\tau} \rangle_i). \quad (16)$$

As already mentioned, $\langle e^{-\tau} \rangle_i$ is the continuum intensity-weighted average of the exponential of the opacity distribution. Therefore, in order to observe variations between normalized absorption spectra, the necessary condition is that the opacity of the absorbing region behind which the continuum changed is different from the overall average opacity; in other words, that the absorbing material has substructures at scales smaller than the continuum illumination solid angle (Ω_{abs}).

Because the function $e^{-\tau}$ takes values strictly between 0 and 1, the most favorable cases to detect variations according to Eq. (16) are: when $\langle e^{-\tau} \rangle_i \sim 1$ and $e^{-\tau_c} \sim 0$, that is when a small and optically thick region is suddenly illuminated over an absorbing medium of mostly very low opacity; or when $\langle e^{-\tau} \rangle_i \sim 0$ and $e^{-\tau_c} \sim 1$, that is when the sudden change of continuum occurs behind an optically thin region, while previously the bulk of the absorption concerned optically thick material. The maximum possible change in the difference of normalized absorption spectra is $\delta I/I_1$.

5.2. Correlation $\text{H}_2\text{O} - \text{CH}$

Assuming that the absorbing material covers the background continuum source entirely ($f_c = 1$), we can directly convert the absorption profile into optical depth from Eq. (11). With this assumption, it is also possible to deconvolve the hfs pattern of the CH doublets, for example using a Clean algorithm method assuming that the relative intensities of the hfs components follow their statistical weights. Accordingly, we can investigate the optical-depth correlation between the H_2O and CH lines, as shown in Fig. 18 for both the SW and NE lines of sight.

In the Milky Way, both H_2O and CH are found to be excellent tracers of the H_2 along diffuse molecular sightlines. Sheffer et al. (2008) derive a quasi-linear relationship between the column densities of CH and H_2 , with an average abundance ratio of $[\text{CH}]/[\text{H}_2] = 3.5^{+2.1}_{-1.4} \times 10^{-8}$ along diffuse molecular sightlines and dark clouds. For water, Flagey et al. (2013) also find a remarkably constant abundance ratio relative to H_2 in Galactic translucent clouds, with $[\text{H}_2\text{O}]/[\text{H}_2] = (4.8 \pm 0.3) \times 10^{-8}$. Taking these relative abundances with their uncertainties, and assuming (i) that the relative abundances of H_2O and CH for the absorbing material in the PKS 1830–211 absorber are similar to the Galactic clouds, (ii) an ortho-to-para ratio of three for H_2O , and (iii) that the molecules are at excitation equilibrium with cosmic-microwave-background photons ($T_{\text{CMB}} = 5.14 \text{ K}$ at $z = 0.89$, Muller et al. 2013), we would expect opacity ratios $\tau(\text{H}_2\text{O})/\tau(\text{CH}^*)$ of between 3 and 9 (at the 1σ confidence level), CH^* being the normalized CH spectrum (equivalent to a hyperfine structure component of relative strength $S_{\text{ul}} = 1$) obtained after deconvolution of the hyperfine structure of the two CH Λ -doublets.

Discarding the center of the SW line profile (velocities between ~ -10 and $+10 \text{ km s}^{-1}$), for which the water line is heavily saturated and has $f_c \sim 95\%$ (which is therefore not consistent with our working assumption $f_c = 1$), we find that the $\text{H}_2\text{O}/\text{CH}$ opacity ratios along the SW line of sight are roughly around 9 (see also fit results in Table 6), that is, in the upper part of Galactic ratios. Along the NE line of sight, the $\tau(\text{H}_2\text{O})/\tau(\text{CH}^*)$ opacity ratios are somewhat lower than in the SW line of sight, although the spread may partly be due to lower signal-to-noise ratios. These ratios are nevertheless still within the range of values observed in Milky Way translucent clouds. Based on the overall similarity between the $\tau(\text{H}_2\text{O})/\tau(\text{CH}^*)$ ratios in the PKS 1830–211 absorber and in Galactic clouds, and except for the heavily saturated part of the SW water line, we do not find evidence for large opacity effects in other velocity components. Should the source-covering factor be lower than unity for some velocity components, the true optical depth of the water line would rise faster than that of CH, and the points in Fig. 18 would deviate from the straight correlation in the same way as for the saturated region near $v = 0 \text{ km s}^{-1}$. Therefore, regarding H_2O and CH, it seems that the chemical conditions in the different velocity components along the SW line of sight are consistent with a relatively constant $\text{H}_2\text{O}/\text{CH}$ abundance ratio.

Moreover, the differences in H_2O and CH^* opacity ratios between the SW and NE lines of sight follow a similar trend to that observed in the Milky Way between clouds in the central molecular zone (CMZ) and the Galactic disk, for which Sonnentrucker et al. (2013) found a water abundance three to five times higher in the CMZ. The cosmic-ray (CR) ionization rate deduced from a simple analysis of the OH^+ and H_2O^+ ions also follows a similar trend between the CMZ and disk of the Milky Way (Indriolo et al. 2015) on one hand, and the SW and NE lines of sight toward PKS 1830–211 (Muller et al. 2016) on the other. As these ions are precursors of H_2O , the somewhat larger H_2O abundance could be related to a higher CR ionization rate.

6. Summary and conclusions

We monitored the lensed quasar PKS 1830–211 with ALMA over a time span of six months in order to investigate the variability of the submm continuum emission of the blazar and of its foreground molecular absorption. We summarize our results as follows. First, for the continuum activity:

- The submm light curve shows a dramatic and nearly monotonic decrease of 80% in the flux density during our monitoring.
- In contrast, the flux-density ratios between the two lensed images of the quasar show only mild variations of less than 10%. There are signs of variations of the polarization properties, which manifest as fluctuations in the differential polarization between the two images. Toward the end of the monitoring, the quasar seems to have reached a stable stage in its polarization variability.
- The nearly featureless light curve prevents us from obtaining a strong constraint on the time delay between the two images. Looking backwards at the previous measurements of the flux-density ratios, it appears that it is also difficult to precisely determine the differential magnification ratio of the system, as the long-term evolution of the flux-density ratios suggests milli-lensing events on timescales of several years.
- We propose a relatively simple parametric model of a single ballistic synchrotron-cooling plasmon to account for the evolution of the continuum emission during the monitoring.

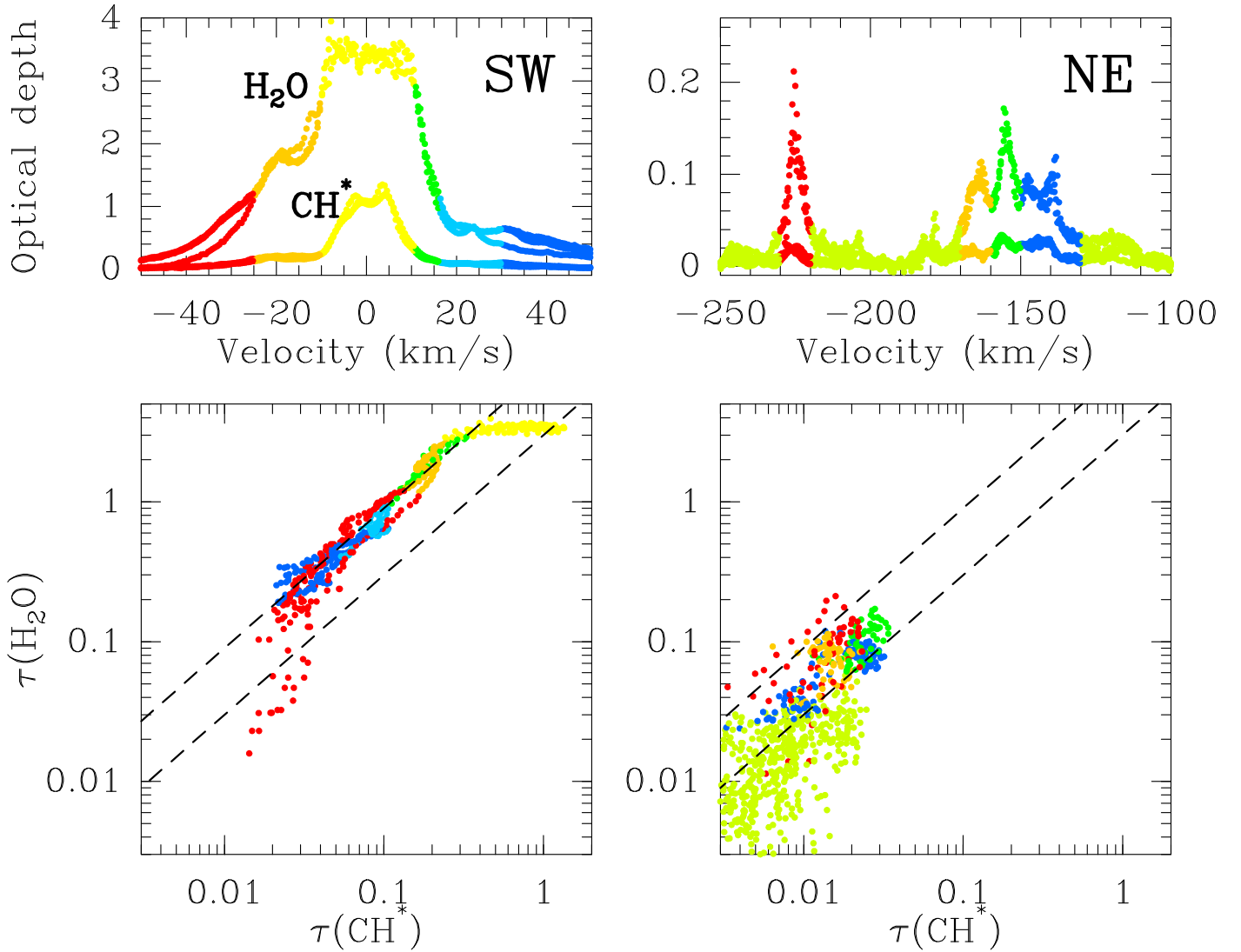


Fig. 18. Correlation between the optical depths of the ortho- H_2O $1_{1,0} - 1_{0,1}$ line and of the deconvolved profile of $\text{CH } 3/2-1/2$ (given for an equivalent hyperfine component with normalized intensity $S_{\text{ul}} = 1$) along the SW (*left*) and NE (*right*) lines of sight, respectively. In both lines of sight, we assume a source-covering factor of $f_c = 1$. The colors encode the velocity intervals shown on the line profiles (*top*). The dashed lines correspond to opacity ratios $\tau(\text{H}_2\text{O})/\tau(\text{CH}^*) = 3$ and 9, respectively.

- From this parametric model, we also obtain a new measurement of the time delay between the NE and SW images of $\Delta t = 25 \pm 3$ days, and of their differential magnification, namely 1.24 ± 0.04 , both of which are consistent with values provided by modeling of the system and its lensing geometry.

For the absorption lines arising in the $z = 0.89$ lens–absorber:

- The absorption line profiles of H_2O (saturated with optical depth >1) and CH (peak opacity $\tau \sim 1$) reveal clear time variations (on average up to $\sim 1\%$ of the continuum level per day for the water line) between spectra taken 1–3 weeks apart.
- A principal component analysis of the absorption spectra toward both images of PKS 1830–211 reveals a seemingly wavy behavior of the variations during the monitoring, with an apparent period of ~ 230 days, although this timescale is longer than the time span of our survey and would therefore need to be confirmed with a longer monitoring. It is tempting to relate this period to the jet precession period of approximately one year in the scenario of a helical jet proposed by

Nair et al. (2005). This would provide a natural explanation for the time variability of the absorption line.

- Combining all the spectra along the SW image, we obtain a detection of the rare isotopolog ^{13}CH , with a $^{12}\text{CH}/^{13}\text{CH}$ ratio of ~ 150 . From complementary data, we also measure oxygen isotopic ratios and derive $^{16}\text{O}/^{18}\text{O} = 65.3 \pm 0.7$ and $^{18}\text{O}/^{17}\text{O} = 11.5 \pm 0.5$.
- We discover a remarkable, broad but shallow absorption trough of 500 km s^{-1} in width observed in the water line toward the SW image, which could be the signature of extra-planar molecular gas.
- We explore the chemical correlation between CH and H_2O using their optical depth ratio and find a $\text{H}_2\text{O}/\text{CH}$ ratio comparable to that observed in Milky Way clouds.

The lens–absorber system toward PKS 1830–211 acts as a powerful cosmological microscope, allowing us to investigate the coupling between the quasar activity and the variations of the absorption pattern. In particular, whether the absorption variability is periodic – and is therefore most likely connected with the precession of the quasar’s helical jet – or irregular – and is

connected to occasional flaring or micro-/milli-lensing events – remains to be confirmed.

Acknowledgements. This paper makes use of the following ALMA data: ADS/JAO.ALMA#2011.0.00405.S (observations of H₂O and CH in April 2012), ADS/JAO.ALMA#2012.1.00056.S (observations of H₂O and CH in May 2014), ADS/JAO.ALMA#2013.1.00020.S (observations of H₂O, CH, H₂¹⁸O, and H₂¹⁷O in July 2014), ADS/JAO.ALMA#2015.1.00075.S (2016 monitoring of H₂O and CH), ADS/JAO.ALMA#2018.1.00051.S (observations of H₂¹⁸O in 2019), ADS/JAO.ALMA#2021.A.00028.S (observations of H₂¹⁸O and H₂¹⁷O in 2022). ALMA is a partnership of ESO (representing its member states), NSF (USA) and NINS (Japan), together with NRC (Canada), NSC and ASIAA (Taiwan), and KASI (Republic of Korea), in cooperation with the Republic of Chile. The Joint ALMA Observatory is operated by ESO, AUI/NRAO and NAOJ. This work has been partially supported by Generalitat Valenciana (GenT Project CIDEAGENT/2018/021 and grant ASFAE/2022/018) and the MICINN (Research Project PID2019-108995GB-C22 and the Astrophysics and High Energy Physics programme, with funding from European Union NextGenerationEU, PRTR-C1711). This research has made use of NASA's Astrophysics Data System.

References

- Abdo, A. A., Ackermann, M., Ajello, M., et al. 2015, *ApJ*, **799**, 143
- Allison, J. R., Moss, V. A., Macquart, J.-P., et al. 2017, *MNRAS*, **465**, 4450
- Bagdonaite, J., Daprá, M., Jansen, P., et al. 2013, *Phys. Rev. Lett.*, **111**, 1101
- Bahcall, J. N., & Spitzer, L., Jr. 1969, *ApJ*, **156**, 63
- Bahcall, J. N., Kozlovsky, B.-Z., & Salpeter, E. E. 1972, *ApJ*, **171**, 467
- Barnacka, A., Glicenstein, J.-F., & Moudou, Y. 2011, *A&A*, **528**, L3
- Barnacka, A., Geller, M. J., Dell'Antonio, I. P., & Benbow, W. 2015, *ApJ*, **809**, 100
- Blandford, R. D., & McKee, C. F. 1982, *ApJ*, **255**, 419
- CASA Team 2022, *PASP*, **134**, 114501
- Cazzoli, G., Puzzarini, C., Harding, M. E., & Gauss, J. 2009, *Chem. Phys. Lett.*, **473**, 21
- Chelouche, D., Pozo-Nunez, F., & Zucker, S. 2017, *ApJ*, **844**, 146
- Combes, F., Gupta, N., Muller, S., et al. 2021, *A&A*, **648**, A116
- Cortes, P. C., Remijan, A., Hales, A., et al. 2022, *ALMA Technical Handbook*, *ALMA Doc. 9.3*, ver. 1.0
- de Nijs, A. J., Ubachs, W., & Bethlem, H. L. 2012, *Phys. Rev. A*, **86**, 2501
- Flagey, N., Goldsmith, P. F., Lis, D. C., et al. 2013, *ApJ*, **762**, 11
- Garrett, M. A., Nair, S., Porcas, R. W., & Patnaik, A. R. 1997, *Vistas Astron.*, **41**, 281
- Guirado, J. C., Jones, D. L., Lara, L., et al. 1999, *A&A*, **346**, 392
- Halfen, D. T., Ziurys, L. M., Pearson, J. C., & Drouin, B. J. 2008, *ApJ*, **687**, 731
- Indriolo, N., Neufeld, D. A., Gérin, M., et al. 2015, *ApJ*, **800**, 40
- Jacob, A. M., Menten, K. M., Wiesemeyer, H., et al. 2020, *A&A*, **640**, A125
- Jauncey, D. L., Reynolds, J. E., Tzioumis, A. K., et al. 1991, *Nature*, **352**, 132
- Jin, C., Garrett, M. A., Nair, S., et al. 2003, *MNRAS*, **340**, 1309
- Kanekar, N., Ubachs, W., Menten, K. M., et al. 2015, *MNRAS*, **448**, 104
- Kobayashi, C., Karakas, A. I., & Umeda, H. 2011, *MNRAS*, **414**, 3231
- Lewis, G. F., & Ibata, R. A. 2003, *MNRAS*, **340**, 562
- Lidman, C., Courbin, F., Meylan, G., et al. 1999, *ApJ*, **514**, 57
- Lovell, J. E. J., Jauncey, D. L., Reynolds, J. E., et al. 1998, *ApJ*, **508**, L51
- Lucas, R., & Liszt, H. 1998, *A&A*, **337**, 246
- Martín, S., Muller, S., Henkel, C., et al. 2019, *A&A*, **624**, A125
- Martí-Vidal, I., & Muller, S. 2019, *A&A*, **621**, A18
- Martí-Vidal, I., Muller, S., Combes, F., et al. 2013, *A&A*, **558**, A123
- Martí-Vidal, I., Vlemmings, W., Muller, S., & Casey, S. 2014, *A&A*, **563**, A136
- Martí-Vidal, I., Muller, S., Vlemmings, W., Horellou, C., & Aalto, S. 2015, *Science*, **348**, 311
- Martí-Vidal, I., Vlemmings, W. H. T., & Muller, S. 2016, *A&A*, **593**, A61
- Martí-Vidal, I., Muller, S., Mus, A., et al. 2020, *A&A*, **638**, L13
- Millon, M., Dalang, C., Lemon, C., et al. 2022, *A&A*, **668**, A77
- Muller, S., & Guélin, M. 2008, *A&A*, **491**, 739
- Muller, S., Guélin, M., Dumke, M., et al. 2006, *A&A*, **458**, 417
- Muller, S., Beelen, A., Guélin, M., et al. 2011, *A&A*, **535**, A103
- Muller, S., Beelen, A., Black, J. H., et al. 2013, *A&A*, **551**, A109
- Muller, S., Combes, F., Guélin, M., et al. 2014, *A&A*, **566**, A112
- Muller, S., Müller, H. S. P., Black, J. H., et al. 2016, *A&A*, **595**, A128
- Muller, S., Müller, H. S. P., & Black, J. H. 2017, *A&A*, **606**, A109
- Muller, S., Jaswanth, S., Horellou, C., & Martí-Vidal, I. 2020a, *A&A*, **641**, L2
- Muller, S., Roueff, E., Black, J. H., et al. 2020b, *A&A*, **637**, A7
- Muller, S., Ubachs, W., Menten, K. M., Henkel, C., & Kanekar, N. 2021, *A&A*, **652**, A5
- Nair, S., Jin, C., & Garrett, M. A. 2005, *MNRAS*, **362**, 1157
- Neronov, A., Vovk, I., & Malyshev, D. 2015, *Nat. Phys.*, **11**, 664
- Oshima, T., Mitsuda, K., Ota, N., et al. 2001, *ApJ*, **551**, 929
- Pacholczyk, A. G. 1970, *Radio Astrophysics. Non-thermal Processes in Galactic and Extragalactic Sources* (San Francisco: Freeman)
- Pedregosa, F., Varoquaux, G., Gramfort, A., et al. 2011, *J. Mach. Lear. Res.*, **12**, 2825
- Prantzos, N., Aubert, O., & Audouze, J. 1996, *A&A*, **309**, 760
- Refsdal, S. 1964, *MNRAS*, **128**, 307
- Schulz, A., Henkel, C., Menten, K. M., et al. 2015, *A&A*, **574**, A108
- Sheffer, Y., Rogers, M., Federman, S. R., et al. 2008, *ApJ*, **687**, 1075
- Sonnentrucker, P., Neufeld, D. A., Gérin, M., et al. 2013, *ApJ*, **763**, 19
- Stanimirović, S., & Zweibel, E. G. 2018, *ARA&A*, **56**, 489
- Tang, X. D., Henkel, C., Menten, K. M., et al. 2019, *A&A*, **629**, A6
- Tercero, B., Cernicharo, J., Cuadrado, S., de Vicente, P., & Guélin, M. 2020, *A&A*, **636**, L7
- Tielens, A. G. G. M. 2005, *The Physics and Chemistry of the Interstellar Medium* (Cambridge: Cambridge University Press)
- Truppe, S., Hendricks, R. J., Hinds, E. A., & Tarbutt, M. R. 2014, *ApJ*, **780**, 71
- Tumlinson, J., Peebles, M. S., & Werk, J. K. 2017, *ARA&A*, **55**, 389
- Valdivia, V., Godard, B., Hennebelle, P., et al. 2017, *A&A*, **600**, A114
- van Ommen, T. D., Jones, D. L., Preston, R. A., & Jauncey, D. L. 1995, *ApJ*, **444**, 561
- Wallström, S. H. J., Muller, S., & Guélin, M. 2016, *A&A*, **595**, A96
- Wambsganss, J. 1992, *ApJ*, **392**, 424
- Wiklund, T., & Combes, F. 1996, *Nature*, **379**, 139
- Wiklund, T., & Combes, F. 1998, *ApJ*, **500**, 129
- Wiklund, T., & Combes, F. 2001, *ASP Conf. Proc.*, **237**, 155
- Winn, J. N., Kochanek, C. S., McLeod, B. A., et al. 2002, *ApJ*, **575**, 103

Appendix A: Spectroscopic data

Spectroscopic data for the transitions of H₂O and CH isotopologs observed in this study are given in Tab. A.1.

Table A.1. Spectroscopic parameters for transitions of H₂O and CH isotopologs observed in this study.

Species	Transition	Rest Freq. (GHz)	Redshifted Freq. (GHz)	S_{ul}	E_{low} (K)
ortho-H ₂ O	$J_{K_a,K_c} = 1_{1,0} - 1_{0,1}$	556.9359877	295.328	4.5	0.0
ortho-H ₂ ¹⁸ O	$J_{K_a,K_c} = 1_{1,0} - 1_{0,1}$	547.676440	290.418	4.5	0.0
ortho-H ₂ ¹⁷ O	$J_{K_a,K_c} = 1_{1,0} - 1_{0,1}$	552.020960	292.722	4.5	0.0
CH	$(J^p, F) = (3/2^+, 1) - (1/2^-, 1)$	532.7215886	282.488	0.17	0.2
	$(J^p, F) = (3/2^+, 2) - (1/2^-, 1)$	532.7238893	282.489	0.83	0.2
	$(J^p, F) = (3/2^+, 1) - (1/2^-, 0)$	532.7932746	282.526	0.33	0.2
	$(J^p, F) = (3/2^-, 2) - (1/2^+, 1)$	536.7610463	284.630	0.83	0.0
	$(J^p, F) = (3/2^-, 1) - (1/2^+, 1)$	536.7818563	284.641	0.17	0.0
	$(J^p, F) = (3/2^-, 1) - (1/2^+, 0)$	536.7955695	284.648	0.33	0.0
¹³ CH	$(J^p, F_1, F) = (3/2^+, 1, 1/2) - (1/2^-, 1, 3/2)$	531.859975	282.031	0.04	0.2
	$(J^p, F_1, F) = (3/2^+, 1, 3/2) - (1/2^-, 1, 3/2)$	531.862711	282.033	0.19	0.2
	$(J^p, F_1, F) = (3/2^+, 1, 1/2) - (1/2^-, 1, 1/2)$	531.910901	282.058	0.05	0.2
	$(J^p, F_1, F) = (3/2^+, 1, 3/2) - (1/2^-, 1, 1/2)$	531.913471	282.060	0.07	0.2
	$(J^p, F_1, F) = (3/2^+, 2, 3/2) - (1/2^-, 1, 3/2)$	532.083360	282.150	0.11	0.2
	$(J^p, F_1, F) = (3/2^+, 2, 5/2) - (1/2^-, 1, 3/2)$	532.086251	282.151	1.00	0.2
	$(J^p, F_1, F) = (3/2^+, 2, 3/2) - (1/2^-, 1, 1/2)$	532.134740	282.177	0.55	0.2
	$(J^p, F_1, F) = (3/2^+, 1, 1/2) - (1/2^-, 0, 1/2)$	532.224939	282.225	0.25	0.1
	$(J^p, F_1, F) = (3/2^+, 1, 3/2) - (1/2^-, 0, 1/2)$	532.227528	282.226	0.41	0.1
	$(J^p, F_1, F) = (3/2^+, 2, 3/2) - (1/2^-, 0, 1/2)$	532.448670	282.343	0.01	0.1
	$(J^p, F_1, F) = (3/2^-, 1, 3/2) - (1/2^+, 0, 1/2)$	536.005094	284.229	0.49	0.0
	$(J^p, F_1, F) = (3/2^-, 1, 1/2) - (1/2^+, 0, 1/2)$	536.024969	284.240	0.17	0.0
	$(J^p, F_1, F) = (3/2^-, 1, 3/2) - (1/2^+, 1, 3/2)$	536.026643	284.241	0.17	0.0
	$(J^p, F_1, F) = (3/2^-, 1, 3/2) - (1/2^+, 1, 1/2)$	536.037944	284.247	0.01	0.0
	$(J^p, F_1, F) = (3/2^-, 1, 1/2) - (1/2^+, 1, 3/2)$	536.046477	284.251	0.04	0.0
	$(J^p, F_1, F) = (3/2^-, 1, 1/2) - (1/2^+, 1, 1/2)$	536.057826	284.257	0.13	0.0
	$(J^p, F_1, F) = (3/2^-, 2, 3/2) - (1/2^+, 0, 1/2)$	536.099484	284.279	0.01	0.0
	$(J^p, F_1, F) = (3/2^-, 2, 5/2) - (1/2^+, 1, 3/2)$	536.101144	284.280	1.00	0.0
	$(J^p, F_1, F) = (3/2^-, 2, 3/2) - (1/2^+, 1, 3/2)$	536.121035	284.291	0.13	0.0
	$(J^p, F_1, F) = (3/2^-, 2, 3/2) - (1/2^+, 1, 1/2)$	536.132344	284.297	0.53	0.0

Notes. Sky frequencies are calculated for $z=0.88582$. For H₂O, the frequency is taken from [Cazzoli et al. \(2009\)](#). For CH, frequencies are taken from [Truppe et al. \(2014\)](#) and line relative intensities (S_{ul}) from [de Nijs et al. \(2012\)](#). Each rotational J -level is split into two opposite parity states ($p = +, -$) by Λ -doubling. The hydrogen nuclear spin ($I = 1/2$) further splits each level into hyperfine components $\mathbf{F} = \mathbf{J} + \mathbf{I}$. For ¹³CH, spectroscopic data are taken from [Halfen et al. \(2008\)](#) and the JPL molecular spectroscopy database. Both nuclei have spin angular momentum. J couples with the ¹³C spin ($I_1 = 1/2$) $\mathbf{F}_1 = \mathbf{J} + \mathbf{I}_1$. Then, F_1 couples with the hydrogen spin ($I_2 = 1/2$): $\mathbf{F} = \mathbf{F}_1 + \mathbf{I}_2$.

Appendix B: Additional material

We provide an overview of the ALMA continuum-normalized absorption spectra of H₂O and CH toward the SW and NE image of PKS 1830–211 during our monitoring in Figs. B.1 and B.2, respectively.

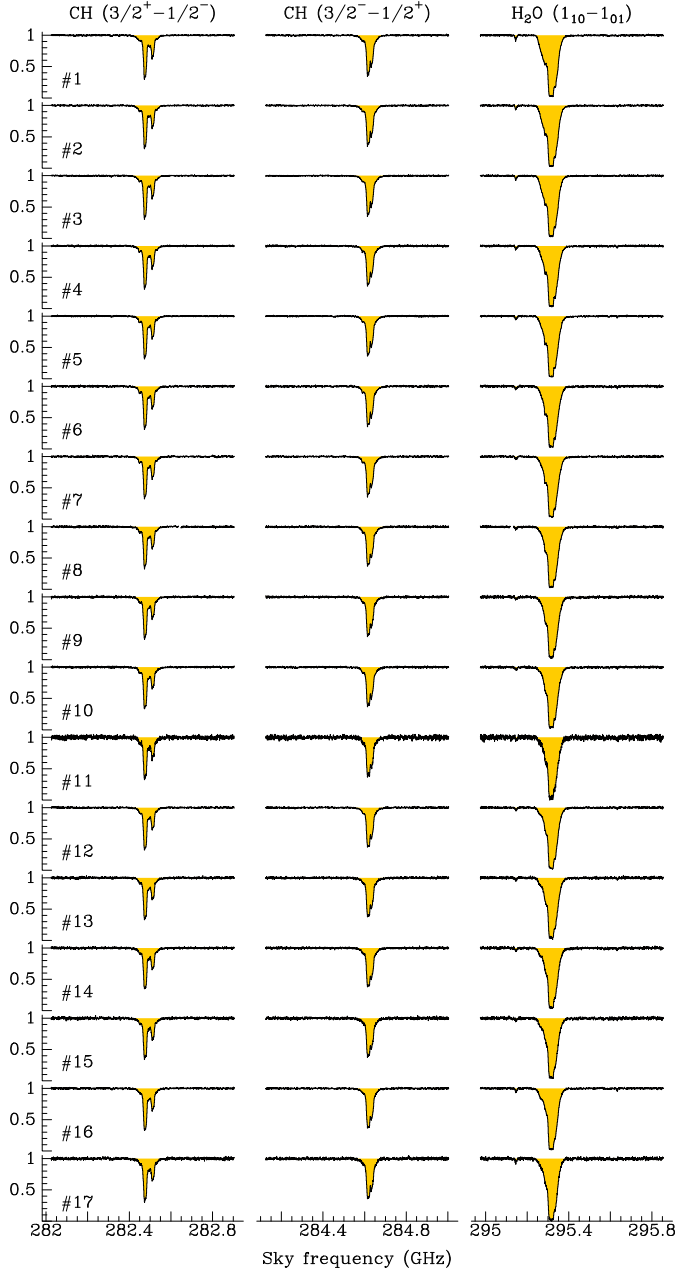


Fig. B.1. Overview of the continuum-normalized absorption spectra of the CH $J^p = 3/2^+ - 1/2^-$ (left), CH $J^p = 3/2^- - 1/2^+$ (middle), and ortho-H₂O $J_{K_a, K_c} = 1_{1,0} - 1_{0,1}$ (right) lines toward the SW image of PKS 1830–211, for each visit of the 2016 monitoring. The visit numbers #i correspond to the entries in Table 1.

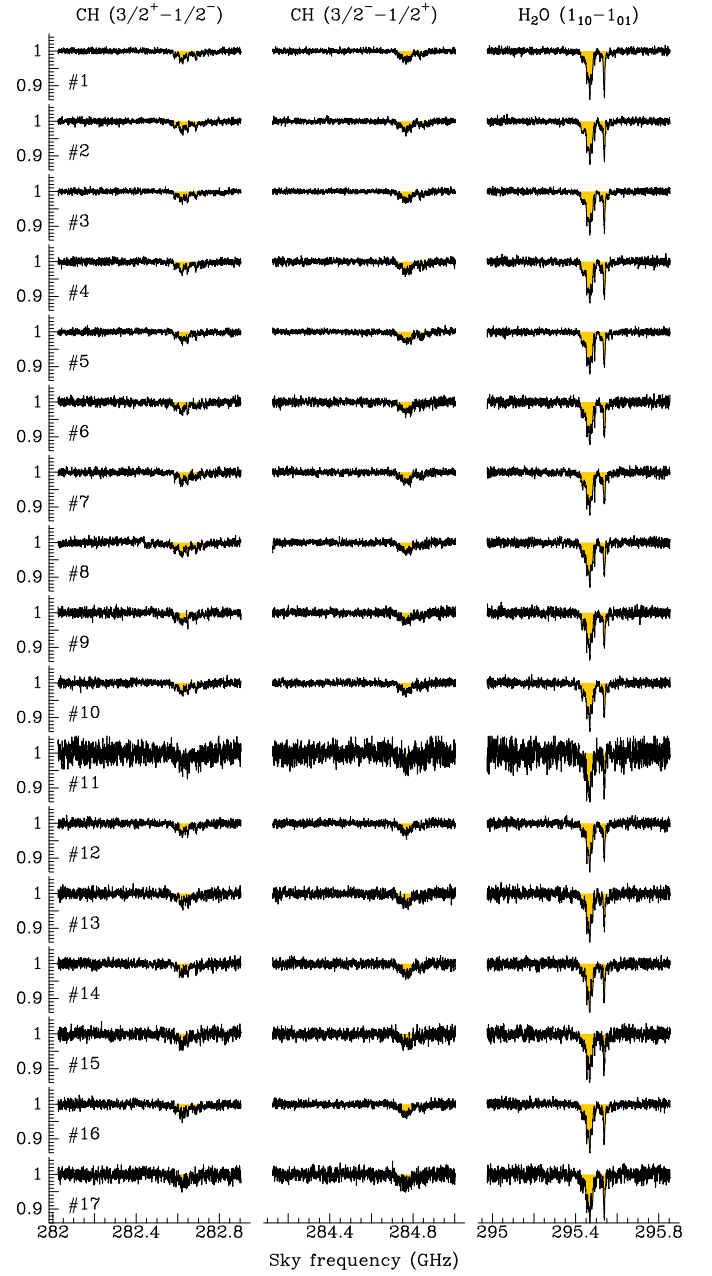


Fig. B.2. Same as Fig. B.1, but toward the NE image of PKS 1830–211.